Study by Optical Spectroscopy of Bismuth Emission in a Nanosecond-Pulsed Discharge Created in Liquid Nitrogen

Anna Nominé, Cédric Noel, Thomas Gries, Alexandre Nominé,, Valentin Milichko, Thierry Belmonte

▶ To cite this version:

> Anna Nominé, Cédric Noel, Thomas Gries, Alexandre Nominé,, Valentin Milichko, et al.. Study by Optical Spectroscopy of Bismuth Emission in a Nanosecond-Pulsed Discharge Created in Liquid Nitrogen. Molecules, 2021, 26 (23), pp.7403. 10.3390/molecules26237403 . hal-03468388

HAL Id: hal-03468388
https://hal.univ-lorraine.fr/hal-03468388

Submitted on 7 Dec 2021

HAL is a multi-disciplinary open access archive for the deposit and dissemination of scientific research documents, whether they are published or not. The documents may come from teaching and research institutions in France or abroad, or from public or private research centers.

L'archive ouverte pluridisciplinaire **HAL**, est destinée au dépôt et à la diffusion de documents scientifiques de niveau recherche, publiés ou non, émanant des établissements d'enseignement et de recherche français ou étrangers, des laboratoires publics ou privés.

Distributed under a Creative Commons Attribution 4.0 International License

Study by Optical Spectroscopy of Bismuth Emission in a Nanosecond-Pulsed Discharge Created in Liquid Nitrogen

Anna Nominé[1], Cédric Noel[1], Thomas Gries[1], Alexandre Nominé[1,2], Valentin Milichko[2] and Thierry Belmonte[1]

[1] Université de Lorraine, CNRS, IJL, F-54000 Nancy, France

[2] ITMO University, St. Petersburg 197101, Russia

Abstract:

Time-resolved optical emission spectroscopy of nanosecond-pulsed discharges ignited in liquid nitrogen between two bismuth electrodes is used to determine the main discharge parameters (electron temperature, electron density, optical thickness). 19 lines belonging to the Bi I system and 7 to the Bi II system could be recorded by plunging directly the optical fibre into the liquid to the close vicinity of the discharge. The lack of data for Stark parameters to evaluate the broadening of Bi I lines was solved by taking advantage of the time-resolved information supported by each line to determine them.

The electron density is found to decrease exponentially from $6.5 \pm 1.5 \times 10^{16}$ cm^{-3} 200 ns after ignition to $1.0 \pm 0.5 \times 10^{16}$ cm^{-3} after 1050 ns. The electron temperature is found to be 0.35 eV, close to the value given by Saha's equation.

Keywords: optical emission spectroscopy; discharges in liquids; bismuth Stark parameters

1. Introduction

Processes based on discharges in liquids are commonly used to synthesize original nano-objects with high yields [1–5]. In liquid nitrogen, they are particularly interesting as they lead to the synthesis of two-dimensional structural materials like nanosheets [6–8], exhibiting high level of selectively exposed reactive facets and fast separation of electrons and holes.

Bismuth trioxide is a semiconducting material with high ionic conductivity and photosensitivity, large energy bandgap and high refractive index, making them useful for various applications as optical coatings, solar or fuel cells, microwave integrated circuits and/or gas sensors [9–12]. Its synthesis as nanosheets by discharges in liquid nitrogen and further oxidation to air has been demonstrated recently.

In the present work, attention is paid on optical emission during the discharge process. By applying a nanosecond-pulsed high-voltage to bismuth electrodes submerged in liquid nitrogen, the erosion process leads to the production of metallic nanosheets. After processing, liquid nitrogen evaporates and nanosheets, exposed to air, get oxidized and are transformed into Bi_2O_3. Diagnosing these discharges is not an easy task as they are very small (tens of micrometres) and pretty fast (hundreds of nanoseconds) [13]. However, such investigations are essential to access to plasma parameters, which is important to improve our control of the process [14–16].

Basic data concerning line broadening for bismuth is relatively unexplored. For instance, if Stark parameters are available for Bi II transitions [17–19], there are missing for Bi I transitions. Discharges in liquids are close to local thermodynamic equilibrium. They are characterized by high electron densities (typically around 10^{16}–10^{17} cm^{-3}), low electron temperatures (below 1 eV) and they are submitted to high pressures (up to several tens of bars in liquid nitrogen). Thus, they are optically thick at inception and lead to non-symmetrical line shapes, self-absorbed transitions and line shifts in wavelength [13].

Methods based on the so-called ‘six free parameters deconvolution’ (SFPD) procedure were developed to determine from experimental data, parameters of given emission lines [20–24]. Here, the broadening parameters of selected bismuth lines are determined together with plasma parameters. We also propose a new way to improve the quality of the raw signals recorded during measurements by introducing the optical fibre directly in the liquid, as close to the discharge as possible.

2. Materials and Methods

The experimental set-up was presented in detail in reference [25]. Briefly, a pin-to-pin electrode configuration was used. Electrodes were bismuth rods (5 mm in diameter – 99.9 % purity) cut to sharp points (curvature radius: 100 µm – **see Figure 1**). A high DC voltage power supply (Technix SR15-R-1200–15 kV–80 mA) fed a solid-state switch (Behlke HTS-301-03-GSM) connected to one pin-electrode, the other electrode being grounded. The voltage rise time was 20 ns without ballast resistor. The applied voltage is +10 kV and the current reaches a maximum of 60 amperes. The voltage pulse width is 75 ns. The energy dissipated in average per pulse is between 1 and 5 mJ, typically.

Optical emission spectroscopy was performed with a 550 mm focal length monochromator (Jobin–Yvon TRIAX 550) equipped with a 100 gr. mm^{-1} grating blazed at 500 nm for overall spectra in the visible range (250–900 nm). For the time evolution of specific lines, a 1800 gr. mm^{-1} grating blazed at 330 nm was used, also in the range (250–900 nm). It was coupled with a HORIBA Jobin–Yvon i-Spectrum Two iCCD detector. The iCCD detector is triggered by the trigger output of the oscilloscope, which is itself triggered by the current peak. Each measurement is averaged over 50 spectra recorded with an exposure time of 50 ns. The iCCD gain is always set to its maximum. Although discharges in dielectric liquids are known to be stochastic, using a solid-state switch with a 20-ns rise time ensures a high level of reproducibility because breakdown necessarily occurs within a time window inferior to the exposure time. However, because of the generation of high-frequency signals by discharge current oscillations (at about 1 MHz), ghost lines are sometimes observed. They are easily identified in time-resolved data, since they disappear from one spectrum to the other.

In this work, light is collected through a multi-strand optical fibre. Because of the weakness of the emitted light when the fibre is out of the liquid, decision was made to strip the metallic tip of the fibre and to plunge the non-conductive strands, tied together by a Teflon tape, directly into liquid nitrogen as close to the discharge as possible. Processing this way enables a strong increase in line intensity and makes ionic lines (Bi II system) appear in the spectra (**Figure 2**). All ionic lines but the one at 430.17 nm are nonetheless very weak and only visible from 200 to 350-400 ns after breakdown with the 100 gr. mm^{-1} grating. Though nanoparticles are produced by electrode erosion, deposition on the fibre is negligible. It is certainly because of shockwaves emitted during the very early stage of the discharge process that push nanoparticles away from the interelectrode gap.

Transitions belonging to the Bi I and Bi II systems were identified during this study. They are listed in **Table 1** (see **supplemental material 1** for the visualization of transitions in corresponding Grotrian diagrams) [26, 27]. The last three columns contains data evaluated for the present study from the experimental spectra. The two previous columns are theoretical estimates of C'_3 and C'_6 coefficients. No line beyond 500 nm was observed. Some lines are too weak or too noisy to be accurately treated. Lines are considered as being weak with regards to their intensity as recorded by the selected optical set-up. Thus, the UV transition at 262.79 nm is strong with the 100 gr. mm^{-1} grating but weak with the more dispersive 1800 gr. mm^{-1} grating. As high resolution is needed for an accurate description, only strong or very strong (see **Table 1**) transitions recorded with the 1800 gr. mm^{-1} grating were modelled, weak or very weak transitions being however considered when mixed with strong lines.

It was not possible in the present conditions to exploit line shifts. Theoretically, at highest electron density found in this work (~6-7×10^{16} cm^{-3}), *i.e.* when lines are strongly broadened and exhibit flat or reversed maxima, the expected line shift is at best 80 pm. With the 1800 gr. mm^{-1} grating used in this work, the distance between two consecutive pixels of the detector corresponds to a wavelength difference of 23 pm.

The lack of nitrogen transition lines in recorded spectra is attributed the optical thickness of the medium as discussed in reference [2]. Ground states are highly populated, leading to light trapping in the medium. Lower states of Bismuth transitions, conversely, are weakly populated states, enabling the exit of light out of the medium.

3. Theory

The theoretical aspects supporting the present study are described in detail in two publications of ours [13, 28]. A short version, presenting only the elements required for the present work, is provided for the sake of clarity.

Basically, optical transitions in spark discharges in liquids are broadened by various phenomena whose relative weights change in time because of the rapid evolution of the most important parameters that control the discharge. The electron temperature, the electron density, the total pressure and the medium optical thickness are known to strongly vary at the very beginning of the process, *i.e.* from 0 to ~20-25 ns, more moderately from 25 to 150-200 ns when the current drops and then only weakly beyond 200 ns when it oscillates.

Before describing the mechanisms responsible for line broadening, an optical model is needed to account for the trapping of a part of the emitted light.

3.1. Optical model

When a photon is emitted by an electronic transition between an upper level and a lower level, if it travels through a medium in which the concentration of the species standing in the lower level is high enough, it will be absorbed and emitted again several times. The trapping probability depends on the wavelength of the photon. If it matches the energy transition, *i.e.* if it has a wavelength corresponding to the line center rather than the line wings, it will be higher. This leads to a depletion in photons and a hole in the center of the energy distribution (see **supplemental material 2**).

The spectral density of the radiant flux (expressed in W m^{-2} Hz^{-1} sr^{-1}) depends on the photon frequency *v* and on the distance from the discharge center *r*:

$$dI(r,\nu) = \big(\varepsilon(r,\nu) - \kappa(r,\nu)I(r,\nu)\big)dr. \tag{1}$$

Absorption $\kappa(r,\nu)$ [m^{-1}] and emission $\varepsilon(r,\nu)$ [W m^{-3} Hz^{-1} sr^{-1}] coefficients are determined from Einstein's coefficients for spontaneous emission A_{ul}, photo-absorption B_{lu} and induced emission B_{ul}:

$$\varepsilon(r,\nu) = \frac{A_{ul}n_u(r)h\nu_0}{4\pi}f(r,\nu) \tag{2}$$

$$\kappa(r,\nu) = \frac{[B_{lu}n_l(r) - B_{ul}n_u(r)]h\nu_0}{c}f(r,\nu), \tag{3}$$

where $n_l(r)$ et $n_u(r)$ are the densities of the lower and upper levels of the transition. $f(r,\nu)$ is the normalized spectral distribution for an atomic transition at a given position *r*: $\int_{-\infty}^{+\infty} f(r,\nu)d\nu = 1$.

In discharge in liquids, Planck's emission dominates at the beginning of the process (see paragraph 3.2). This specific contribution, denoted $\varepsilon_{bg}(r,\nu)$, superimposes upon line emission and Eq. (2) changes to :

$$\varepsilon(r,\nu) = \frac{A_{ul}n_u(r)h\nu_0}{4\pi}f(r,\nu) + \varepsilon_{bg}(r,\nu). \tag{4}$$

The transition probability for induced emission is given by $B_{ul} = (c/\nu_0)^3(A_{ul}/8\pi h)$ and it is related to B_{lu} by $B_{lu} = (g_u/g_l)B_{ul}$ where g_u and g_l are the degeneracy degrees of the upper and lower levels. The intensity of the radiant flux is obtained by integration of Eq. (1) over the photon path:

$$I(\nu) = \frac{1}{exp\left[-\int_{-\infty}^{+\infty} \kappa(r,\nu)dr\right]} \int_{-\infty}^{+\infty} exp\left[-\int_{-\infty}^{+\infty} \kappa(r,\nu)dr\right] \varepsilon(r,\nu)dr. \quad (5)$$

Therefore, a spatial density distribution is needed. For electrons and neutral species, a Gaussian distribution is commonly chosen for discharges exhibiting a cylindrical symmetry [29, 30]:

$$n_e(r) = N_e(0)\, exp\left(\frac{-r^2}{\sigma_e^2}\right);\;\; n_u(r) = N_u(0)\, exp\left(\frac{-r^2}{\sigma_u^2}\right);\;\; n_l(r) = N_l(0)\, exp\left(\frac{-r^2}{\sigma_l^2}\right). \quad (6)$$

Standard deviations may be specific to each specie. For the sake of simplicity, and to decrease as much a possible the number of parameters in the model, we set: $\sigma_e^2 = \sigma_u^2 = \sigma_l^2$. Assuming a Boltzmann distribution between energy levels leads to: $\frac{N_u(0)}{N_l(0)} = \frac{g_u}{g_l} exp\left(\frac{-h\nu_0}{k_B T_e}\right)$. Such profiles are not physical because they do not take into account radial gradients of electron temperature and gas pressure. As these data are unknown in the present condition, the simplest description was adopted to account for optical thickness of emission lines.

3.2. Line broadening

Because of the heavy mass of bismuth (M = 208,98 u), line broadening mechanisms are essentially limited to resonance broadening for the only transition at 306.77 nm and to instrumental and Stark broadenings for all transitions. Indeed, Doppler and van der Waals (both in the quasi-static and impact approximations) broadenings remain at negligible levels, these contributions being systematically evaluated (see reference [13] for formula used in that purpose). In Table 2, the various possible contributions to broadening for different lines are given for $n_e = 6\times10^{16}$ cm^{-3}. 3 main contributions are to be considered: instrumental, resonance and Stark broadenings.

The instrumental broadening was found equal to 0.10 nm thanks to a calibration using a He-Ne laser. The line shape thus obtained was approximately Gaussian.

The transition at 306.77 nm is resonant as it involves an upper level directly dipole-coupled to the ground state (the electric dipole transition and the corresponding force derives from the potential $\Delta V_3 = \hbar C_{3,gl}/r^3$). At low densities, lines broadening by resonance adopt Lorentzian shape. The full width at half maximum (FWHM) is given by:

$$\Delta\nu_{res} = \pi k_{gl} C'_{3,gl} \sqrt{\frac{g_g}{g_l}} N_g. \quad (7)$$

k_{gl} is a numerical constant for the transition between the lower level and the ground level. We used $k_{gl} = 1.53$ [31]. N_g is the density of the ground state. The coefficient $C'_{3,gl}\ [m^3 \cdot s^{-1}]$ can be evaluated from the oscillator strength f_{gl} with:

$$C'_{3,gl} = \frac{C_{3,gl}}{\hbar} = \frac{1}{4\pi}\frac{1}{4\pi\varepsilon_0}\frac{e^2}{m_e}\frac{f_{gl}}{\nu_{\mathrm{lg}}}, \quad (8)$$

and:

$$f_{gl} = \frac{C_{3,gl}}{\hbar} = \frac{4\pi\varepsilon_0}{8\pi^2}\frac{c^3 m_e}{e^2\nu_{lg}^2}\frac{g_l}{g_g} A_{lg}. \quad (9)$$

Constants have their usual meaning.

C_6' coefficients were also estimated (see Table 1 and ref. [28]) using the following expression:

$$C_6' = \frac{2\pi e^2}{4\pi\varepsilon_0 h}\alpha|\langle R_u^2\rangle - \langle R_l^2\rangle|a_0^2. \tag{10}$$

where α is the polarizability of the emitter, $\langle R_u^2\rangle$ the mean square radius of the atom in its excited level *j* and a_0 the Bohr radius.

Stark profiles are produced under the action of high-frequency fields of electrons (the linear Stark effect obeys a potential $\Delta V_2 = -\hbar C_2/r^2$) and under the action of the low-frequency fields of ions (the quadratic Stark effect with $\Delta V_4 = -\hbar C_4/r^4$). In the case of non-hydrogenoid atomic transition, ion broadening is not negligible and line profiles become asymmetric, as it is clearly the case with bismuth. Within the quasi-static approximation , the line profile is given by:

$$j_{A,R}(x) = \frac{1}{\pi}\int_0^\infty \frac{H_R(\beta)}{1+\left(x-A^{4/3}\beta^2\right)^2}d\beta, \tag{11}$$

where $x = \frac{\lambda-\lambda_0-d_e}{w_e}$, w_e is the half width at half maximum (HWHM) of the Stark broadening due to electron collision and d_e is the corresponding shift. $H_R(\beta)$ is the distribution function of the micro-field intensity that depends on the normalized intensity of the Holtsmark field $\beta=F/F_0$, F_0 being the intensity of the normal field. *A* is the broadening parameter due to static ions. *R* is the ratio of the average distance between ions and the Debye radius, *i.e.* the screening parameter of Debye:

$$R = \left[\frac{36\pi e^6 n_e}{(k_B T_e)^3}\right]^{1/6} \approx 0.0899\frac{\left(n_e[cm^{-3}]\right)^{1/6}}{T_e^{1/2}}. \tag{12}$$

The expression of $j_{A,R}(x)$ is determined thanks to the Woltz tables [32] from w_e. When the ion dynamics is no longer negligible, it is necessary to introduce a correction factor. The criterion to fulfill is then [20]:

$$B = A^{1/3}\frac{8.06\times10^{-7}w_e^{ref}[nm]}{(\lambda[nm])^2}(n_e[m^{-3}])^{2/3}\sqrt{\frac{\mu[amu]}{T_g[K]}} < 1, \tag{13}$$

where w_e^{ref} is the value of w_e when $n_e = 10^{23}$ m^{-3}. μ is the reduced mass of the ion or neutral perturber in arbitrary mass unit. This means that strong collisions due to electrons and ions are well separated in time. Then, the total broadening is given by:

$$\Delta\lambda_s = 2w_e\left[1 + 1.75AD_J(1-0.75\kappa R)\right] \tag{14}$$

with $D_J = \frac{1.36}{1.75(1-0.75R)}B^{-1/3}$ if $B < \left(\frac{1.36}{1.75(1-0.75R)}\right)^3$ or $D_J = 1$ if $B \geq \left(\frac{1.36}{1.75(1-0.75R)}\right)^3$ [20]. In this latter case, ion dynamics is negligible and the line shape is treated by considering the quasi-static approximation.

Approximate formulas, resorting to parametric functions, were derived for an easier use. They are reasonably accurate if $0.05 \leq \alpha \leq 0.5$ and $r \leq 0.8$, these two quantities being defined hereafter. The line width broadened by Stark effect is then given by:

$$\Delta\lambda_s = 2[1 + 1.75\alpha(1-0.75\kappa r_D)]w, \tag{15}$$

where $w(T_e, n_e)$ and $\alpha(T_e, n_e)$ are two parametric functions tabulated by [33]. They represent the electronic contribution expressed in wavelength and the ion quasi-static broadening parameter. They scale respectively as n_e and $n_e^{1/4}$. So, they are more conveniently written as $w(T_e, n_e) = \frac{n_e}{n_e^0} w_e(T_e)$ and $\alpha(T_e, n_e) = \left(\frac{n_e}{n_e^0}\right)^{1/4} a(T_e)$ where w_e and a are dependent on T_e only. n_e^0=10^{22} m^{-3}. $r_D = \rho_m/\rho_D$ is the Debye shielding parameter. It is the ratio of the mean distance between ions $\rho_m = \left(\frac{4}{3}\pi n_e\right)^{-1/3}$ and the Debye radius $\rho_D = \sqrt{\frac{\varepsilon_0 k_B T_e}{e^2 n_e}}$. $r_D \approx 8.899 \times 10^{-3} n_e^{1/6} T_e^{-1/2}$. κ is a constant equal to 1 for a neutral emitter and 1.6 for an ion emitter. Equation (14) reads:

$$\Delta\lambda_s = 2 \times 10^{-22}\left[1 + 5.534 \times 10^{-6} n_e^{1/4} a(T_e)\left(1 - 6.742 \times 10^{-3} \kappa n_e^{1/6} T_e^{-1/2}\right)\right] \times n_e w_e(T_e). \qquad (16)$$

3.3. Line intensity

The intensity I_{ul} of each line is related with the energy of the upper emitting level through the following equation:

$$ln\left(\frac{I_{ul}}{A_{ul} h \nu_{ul}}\right) = \left(-\frac{1}{k_B T}\right) E_u - ln\left(\frac{4\pi Q(T)}{N_0 g_u V \Omega R(\nu)}\right) \qquad (17)$$

$Q(T)$ is the partition function, which depends on the temperature, Ω is the solid angle through which the emitting volume V is observed. $R(\nu)$ is the optical response of the device which is dependent on the wavelength. So, the intensity ratio of 2 lines is given by:

$$\frac{I_1}{I_2} = \frac{A_1 g_{u1} R(\nu_1) \nu_1}{A_2 g_{u2} R(\nu_2) \nu_2} exp\left(\frac{E_2 - E_1}{k_B T}\right) \qquad (18)$$

It is useful to introduce the following parameter:

$$\rho = \frac{I_1^{theo}/I_{ref}^{theo}}{I_1^{exp}/I_{ref}^{exp}} \qquad (19)$$

By choosing a given reference line, it is possible to determine with Eq. 18 the theoretical ratio of the intensity of any other line to the intensity of this one. Its comparison with the same experimental ratio through the parameter ρ indicates whether the upper levels are populated according to a Boltzmann distribution or not. ρ is then expected to be equal to 1. If ρ is large, the intensity of the selected line is weaker than expected with regards to the intensity of the reference line.

3.4. Applied method

In this work, the broadening parameters of 12 among 14 selected lines of bismuth are determined (2 are too weak to determine their broadening parameters). High-pressure lamps are often preferred in that purpose, as more accurate parameters for line transitions can be obtained. Indeed, the reproducibility of discharges in liquids, and therefore the corresponding dynamics, is usually weak, as discussed hereafter. Here, our main concern is first and foremost the evolution of plasma parameters in dense media where this kind of information is rarely available straightforwardly.

To have access to the best information available, the following strategy was adopted. For a given transition, 21 spectra (each being the average of 50 spectra recorded with an exposure time of 50 ns) were recorded every 50 ns from 50 to 1050 ns. 6 spectra were selected among these 21, first to describe at best the time evolution observed in average and second to limit the number of data to process. This selection is made on the intensity of the recorded transition, the more pronounced it is, the best it is. It does not take into account the intensity of the background.

The spectra at shortest times (from 50 to 150 ns) adopt the shape of a continuum emission without visible atomic transition. Because of this, selected lines could only be fitted from 200 ns to 1050 ns. On this basis, the description of the time evolution of each selected line is subjected to a simple rule: decrease as much as possible the number of degrees of freedom, to avoid overparameterization of the problem and get reliable solutions. Time-resolved spectra are thus exploited to check the reliability of the extracted data. Free parameters are then:

- the basic parameters required in Eq. (16) — w_e, d_e and $a(T_e)$ — to account for Stark broadening (see Table 2). These three parameters are usually set with one spectrum, as the broadening, the position of the maximum and the shape of a given line fully determines w_e, d_e and $a(T_e)$,
- the electron density. This variable must decrease in time according to the same law (basically, an exponential decay for a first-order process) whatever the lines,
- the intensity of the continuum emission. This variable must also decrease in time (basically as $t^{-4/3}$ for a solid body cooling down) and follow the time evolution of the continuum.

4. Results and discussion

The discharge pressure has no significant influence on line broadening, as explained already, and it can be arbitrarily set between 5 and 10 bars without affecting results. We chose 5 bars, a realistic value at this stage of the discharge evolution [34], *i.e.* in the time range investigated in this work. Indeed, the pressure decays quickly. So, initial pressures, ranging from tens to hundreds of bars, drop in tens of nanoseconds to a few bars only. This time range spans from 100 to 1050 ns, but practically it reduces from 200 ns to 1050 ns as lines cannot be modelled at short times where the medium is optically thick. The electron temperature was also assumed to be constant as a change by a factor of ten of the electron density only affects the electron temperature by 10% according to Saha's equation. We chose $T_e = 0.35$ eV. This value came up naturally, higher values leading to unrealistic broadenings. It is lower than electron temperatures usually estimated in the same kind of discharges, that lie rather between 0.5 and 1 eV. The reason for this is due to the conditions that prevail in these kinds of discharges: assuming that the medium is close to local thermodynamic equilibrium (LTE), Saha's equation applied to bismuth indicates that if the electron density is 1×10^{16} cm^{-3}, the electron temperature should be 0.37 eV only, which is compliant with the present estimate. Resorting to Saha's equation is not illegitimate, even though discharges in the present conditions are probably closer to equilibrium at short times. Discharges in liquids, behaving as arc or spark discharges at high currents, are known to be close to LTE [35, 36]. In this case, emissive states must follow a Boltzmann distribution (depicted in **Supplement material 3** for the present case), which is also an assumption needed in the optical model.

By following 14 transitions, we could determine the time evolution of the discharge parameters as well as the Stark parameters – w_e, d_e and $a(T_e)$ – (**Table 1**). The accuracy of Stark data derived from the present study is first defined by the coherency of the set of time-resolved spectra. This aspect was evaluated qualitatively. Accuracies given in **Table 1** range from C to E on a scale from A to E as that used by NIST for line transition. It is also dependent on the accuracy of the model used to describe the discharge as it only takes into account a very simplified approach of this complex medium. As no model of discharge in liquids in our conditions has ever been made, quantifying the accuracy of the present values could only be made by comparison with other published data. However, Stark data for transitions belonging to the Bi I system are not available, to the best of the authors' knowledge. Only data for transitions belonging to the Bi II system are available.

Concerning the different modelled transitions, 2 examples are selected here (**Figures 3 and 4**). Other transitions are available as **Supplemental materials 4a to 4h**. The following comments can be made:

- The agreement between experimental values and the theoretical profiles is very satisfactory. It could be even better by changing parameters that were set once and for all in the treatment process according the employed method. Line position, asymmetry, reversal and broadening are well rendered. Of course, the less satisfying profiles are those where information is the noisiest, *i.e.* at short times. It is very clear for the transition at 302.46 nm where data before 750 ns could not be modelled (**Supplemental material 4d**). On the contrary, intense isolated lines at 289.80, 351.09, 359.61, 412.17 and 472.25 (**Supplemental materials 4a and 4e to 4h**) are very well fitted.
- Minor contributions to a main transition by weak lines (at 307.67 nm for the transition at 306.77 nm (**Figure 3**), at 340.28 nm and 340.53 nm for the transition at 339.72 nm (**Figure 4**) and at 299.33 nm for the transition at 298.90 nm (**Supplemental material 4c**)) are needed to describe accurately the whole profile. It is also true for the blue wing of the transition at 293.83 to which the red wing of the transition at 289.80 contributes (**Supplemental material 4b**), and the red wing of the transition at 302.46 nm to which the blue wing of the transition at 306.67 nm contributes as well (**Supplemental material 4d**).
- The fact that the transition at 306.77 nm is resonant (**Figure 3**) makes a double reversal of the line (*i.e.* a small bump in the hole of the line), which is not observed for other transitions. Experimentally, this double reversal is not clear but not unlikely anyway (**Supplemental material 5**). This double reversal comes for the fact that the photons of the continuum are trapped by a lower level implied in a transition where a hole already exists at its central wavelength because the transition is resonant.
- All asymmetric lines have their blue wing expanded except the one at 351.09 nm whose red wing is expanded – **Supplemental material 4e**). The singular behaviour of the transition at 351.09 nm is unexplained.
- The accuracy of the profiles of the weak lines at 307.67 nm, 340.28 nm and 340.53 nm is naturally limited even though their presence improves the profile of the set they

form with the intense line they neighbour. It is important here to mention that these lines should spring up even more in the spectrum than they do (*e.g.* **Figure 4**) if they were not broadened by Stark effect.

From the previous results, the time evolution of the electron density is deduced (**Figure 5**). The density decreases from 6.5 ± 1.5 × 10^{16} cm^{-3} at 200 ns to 1.0 ± 0.5 × 10^{16} cm^{-3} at 1050 ns. The spread of the data is limited, which gives a certain confidence in these results.

The intensity of the continuum emission, as a parameter of the model, may be compared with the experimental data. Indeed, this data is needed in the optical model through the term $\varepsilon_{bg}(r,\nu)$ in Eq. 4. Then, we can compare the time evolutions of this normalized parameter and the normalized experimental value. This is an assessment of the reliability of the optical model. For one line at a given time, the background intensity is evaluated as the value of the linear baseline of the peak at the centre of the selected peak. A set of time values for the background intensities of a given line are then derived by this method. This set of time values is normalized and compared next to those used in the model are normalized as well. **Figure 6** shows the time evolution of the normalized intensity of the continuum for all selected Bi I transitions at the 6 chosen times. Normalized experimental values are compared to the parametric values used in the model. Except for lines at 306.77 nm and 359.61 nm, the agreement is in average very satisfactory.

The time evolution of the different lines belonging to the bismuth I and II systems was studied with the 100 gr. mm^{-1} grating between 50 and 550 ns to take into account all the observed lines and benefit from higher intensities. For the sake of clarity, modelled transitions belonging to the Bi I system (from 289 to 472 nm) are presented before the 5 weak UV (from 262 to 281 nm) and ionic transitions. Close lines (at 298.90 and 299.33 nm, at 306.77 and 307.67 nm and at 339.72, 340.28 and 340.53 nm) are treated here as single lines, only the parameters of the most intense line of the set being considered.

Results concerning transitions from 289 to 472 nm in the Bi I system are showed in **Figure 7**. In **figure 7A**, the time evolution of the intensity of each line is depicted. Except transitions at 412.17 and 472.5 nm that reach their maximum after 400 ns, all other lines behave similarly, with a maximum at 300 ns.

In **Figure 7B**, the time evolution of the ratio of the intensity of a given line X to the intensity of the line at 339.72 nm is given. It is used to compare the time evolution of the most energetic transitions (at low wavelengths) to the less energetic transitions (at high wavelengths). It is quite constant and relatively close to 1 for all transitions in time, confirming the negligible variation of the electron temperature. The evolution at 200-250 ns of the group of 5 lines within the wavelength range [289-307 nm], where I(X) / I(339.72) exceeds 3, is due to a higher continuum emission than expected. This could be caused by a slightly higher electron temperature during these specific measurements. We also notice that all data at 350 ns are weaker than expected, probably also for a reason of weak reproducibility, intrinsic to this process.

The comparison with intensity ratios determined by assuming a Boltzmann distribution from available data leads to an acceptable agreement (the ratio ρ between theory and experiment is between 0.25 and 1.51) for all lines but two: the one at 306.77 nm (ρ = 158) and the one at 472.14 nm (ρ = 50.1). The most striking feature about these two lines is that they are emitted from the resonant level lying at 4.04 eV. Experimentally, the measured intensity is then much lower than expected. The apparent lifetime of the state is increased by the optical thickness of the medium, which could explained the lowering of the intensity of transitions coming from the $6p^2$ ($^3P_0$) $7s_{1/2}$ level.

The 5 UV lines from 262.79 nm to 280.96 nm (**Supplemental material 6A**) were not modelled as their intensities were too weak with the 1800 gr. mm^{-1} grating. The time evolution of the intensity of these lines, established with the 100 gr. mm^{-1} grating, shows that the maximum is reached at about 300 ns (**Supplemental material 6B**), like for most other neutral lines.

The comparison with intensity ratios determined by assuming a Boltzmann distribution from available data (inset in **Supplemental material 6B,** reference line is taken at 262.79 nm) leads to an acceptable agreement (the ratio ρ between theory and experiment is between 1.2 and 2.6) for all lines but the one at 273.05 nm ($\rho = 33.13$). For this latter, the adopted A_{ul} value is 2.02×10^7 s^{-1} (**Table 1**). This value was determined by Stanek *et al.* [37]. To get the same agreement as the other lines, it should be about $2–3\times10^8$ s^{-1}. As the upper level of this transition is very close to the ionization potential (7.225 eV vs 7.285 eV, the lower intensity observed experimentally could possibly be due to an easy loss of this state by ionization.

The two weak ionic lines at 379.25 nm and 430.17 nm were treated alike (**Supplemental material 7A**). The time evolution of the line at 430.17 nm shows that the maximum intensity is reached after 450 ns, against 250 ns for the other ionic line, demonstrating different excitation mechanisms. Line intensities are nevertheless proportional until 250 ns. This observation cannot be exploited by lack of data on A_{ul} for these transitions.

5. Conclusion

The derivation of Stark data for Bi I lines is a convenient way to access discharge parameters, even though the obtained data is not as accurate as it would be with more conventional methods. The resulting values of the parameters show that the discharge is close the thermodynamic equilibrium.

The possibility of using an optical fibre directly in the liquid opens up the way to new perspectives. The recording of enhanced intensity signals improves the quality of experimental results and may bring complementary new information. In this first attempt, the presence of lines belonging to the Bi II system has been evidenced, which could not be observed otherwise. Further experiments could benefit from this possibility to access spatially-resolved emission.

6. Acknowledgements

The authors acknowledge the French PIA (programme d'investissements d'avenir) project Lorraine Université d’Excellence (Ref. ANR-15-IDEX-04-LUE) for financial support.

References

1. Kabbara, H.; Ghanbaja, J.; Noël, C. and Belmonte, T. Nano-objects synthesized from Cu, Ag and $Cu_{28}Ag_{72}$ electrodes by submerged discharges in liquid nitrogen. *Mater. Chem. Phys.* **2018**, *217*, 371–378.
2. Kabbara, H.; Ghanbaja, J.; Noël, C. and Belmonte, T. Synthesis of Cu@ ZnO core–shell nanoparticles by spark discharges in liquid nitrogen. *Nano-Structures Nano-Objects* **2017**, *10*, 22–29.
3. Xing, G.; Jia, S. and Shi, Z. Influence of transverse magnetic field on the formation of carbon nano-materials by arc discharge in liquid. *Carbon* **2007**, *45*, 2584–2588.
4. Parkansky, N.; Goldstein, O.; Alterkop, B.; Boxman, R. L.; Barkay, Z.; Rosenberg, Y. and Frenkel, G. Features of micro and nano-particles produced by pulsed arc submerged in ethanol. *Powder Technol.* **2006**, *161*, 215–219.
5. Gang, X. I. N. G.; Jia, S. L. and Shi, Z. Q. The production of carbon nano-materials by arc discharge under water or liquid nitrogen. *New Carbon Mater.* **2007**, *22*, 337–341.
6. Kabbara, H.; Ghanbaja, J.; Noël, C. and Belmonte, T. Synthesis of copper and zinc nanostructures by discharges in liquid nitrogen. *Mater. Chem. Phys.* **2018**, *207*, 350–358.
7. Kim, S.; Sergiienko, R.; Shibata, E.; Hayasaka, Y. and Nakamura, T. Production of graphite nanosheets by low-current plasma discharge in liquid ethanol. *Mater. Trans.* **2010**, *51*, 1455–1459.
8. Hamdan, A.; Kabbara, H.; Noel, C.; Ghanbaja, J.; Redjaïmia, A. and Belmonte, T. Synthesis of two-dimensional lead sheets by spark discharge in liquid nitrogen. *Particuology* **2018**, *40*, 152–159.
9. Qin, F., Li, G.; Wang, R.; Wu, J.; Sun, H. and Chen, R. Template‐free fabrication of Bi_2O_3 and $(BiO)_2CO_3$ nanotubes and their application in water treatment. *Chem. A Eur. J.* **2012**, *18*, 16491–16497.
10. Morasch, J.; Li, S.; Brötz, J.; Jaegermann, W. and Klein, A. Reactively magnetron sputtered Bi_2O_3 thin films: Analysis of structure, optoelectronic, interface, and photovoltaic properties. *Physica Status Solidi A* **2014**, *211*, 93–100.
11. Tudorache, F.; Petrila, I.; Condurache-Bota, S.; Constantinescu, C. and Praisler, M. Humidity sensors applicative characteristics of granularized and porous Bi_2O_3 thin films prepared by oxygen plasma-assisted pulsed laser deposition. *Superlattices Microstructures* **2015**, *77*, 276–285.
12. Bhande, S. S.; Mane, R. S.; Ghule, A. V. and Han, S. H. A bismuth oxide nanoplate-based carbon dioxide gas sensor. *Scripta Materialia* **2011**, *65*, 1081–1084.
13. Belmonte, T.; Kabbara, H.; Noël, C. and Pflieger, R. Analysis of Zn I emission lines observed during a spark discharge in liquid nitrogen for zinc nanosheet synthesis. *Plasma Sources Sci. Technol.* **2018**, *27*, 074004.
14. Li, Z. L., Bonifaci; N., Aitken; F., Denat; A., von Haeften; K., Atrazhev; V. M. and Shakhatov, V. A. Spectroscopic investigation of liquid helium excited by a corona discharge: evidence for bubbles and “red satellites”. *Eur. Phys. J.: Appl. Phys.* **2009**, *47*, 742–750.

15. Pflieger, R.; Ouerhani, T.; Belmonte, T. and Nikitenko, S. I. Use of NH (A 3 Π–X 3 Σ−) sonoluminescence for diagnostics of nonequilibrium plasma produced by multibubble cavitation. *Phys. Chem. Chem. Phys.* **2017**, *19*, 26272–26279.
16. Rond, C.; Desse, J. M.; Fagnon, N.; Aubert, X.; Er, M.; Vega, A. and Duten, X. Time-resolved diagnostics of a pin-to-pin pulsed discharge in water: pre-breakdown and breakdown analysis. *J. Phys. D: Appl. Phys.* **2018**, 51, 335201.
17. Miller, M. H. and Bengtson, R. D. Experimental transition probabilities and Stark broadening for singly-ionized bismuth. *J. Quant. Spectrosc. Radiat. Transfer* **1980**, *23*, 411–415.
18. Dimitrijevic, M. S. and Popovic, L. C. Stark broadening of Bi II lines of astrophysical interest. Astron. Astrophys. Suppl. Series **1993**, *101*, 583–586.
19. Sahal-Bréchot, S.; Dimitrijević, M.S. and Moreau N. STARK-B database **2021**, [online]. http://stark-b.obspm.fr [July 18, 2021]. Observatory of Paris, LERMA and Astronomical Observatory of Belgrade.
20. Milosavljević, V. and Poparić, G. Atomic spectral line free parameter deconvolution procedure. *Phys. Rev. E* **2001**, *63*, 036404.
21. Nikolić, D.; Djurović, S.; Mijatović, Z. and Kobilarov, R. Comment on “Atomic spectral line-free parameter deconvolution procedure”. *Phys. Rev. E* **2003**, *67*, 058401.
22. Nikolić, D.; Djurović, S.; Mijatović, Z.; Kobilarov, R. and Konjević, N. On modeling of the spectral line shape of heavy neutral nonhydrogen-like emitters. *J. Appl. Spectrosc.* **2001**, *68*, 902–910.
23. Milosavljević, V.; Ellingboe, A. R. and Djeniže, S. Measured Stark widths and shifts of the neutral argon spectral lines in 4s–4p and 4s–4p′ transitions. *Spectrochim. Acta B: At. Spectrosc.* **2006**, *61*, 81–87.
24. Ivković, M.; Zikic, R.; Jovićević, S. and Konjević, N. On simultaneous determination of electron impact width, ion-broadening and ion-dynamic parameter from the shape of plasma broadened non-hydrogenic atom line. *J. Phys. B: At. Molec. Opt. Phys.* **2006**, *39*, 1773–1785.
25. Hamdan, A.; Noel, C.; Kosior, F.; Henrion, G. and Belmonte, T. Impacts created on various materials by micro-discharges in heptane: Influence of the dissipated charge. *J. Appl. Phys.* **2013**, *113*, 043301.
26. Caiyan, L.; Berzinsh, U.; Zerne, R. and Svanberg, S. Determination of radiative lifetimes of neutral bismuth by time-resolved uv-vuv laser spectroscopy. *Phys. Rev. A* **1995**, *52*, 1936–1941.
27. Kramida, A., Ralchenko, Yu., Reader, J., and NIST ASD Team (2021). NIST Atomic Spectra Database (ver. 5.8), [Online]. Available: https://physics.nist.gov/asd [2021, July 31]. National Institute of Standards and Technology, Gaithersburg, MD. DOI: https://doi.org/10.18434/T4W30F
28. Belmonte, T.; Noël, C.; Gries, T.; Martin, J. and Henrion, G. Theoretical background of optical emission spectroscopy for analysis of atmospheric pressure plasmas. *Plasma Sources Sci. Technol.* **2015**, *24*, 064003.
29. Sakka, T.; Nakajima, T. and Ogata, Y. H. Spatial population distribution of laser ablation species determined by self-reversed emission line profile. *J. Appl. Phys.* **2002**, *92*, 2296–2303.

30. Tortai, J. H., Bonifaci, N., Denat, A., & Trassy, C. (2005). Diagnostic of the self-healing of metallized polypropylene film by modeling of the broadening emission lines of aluminum emitted by plasma discharge. *J. Appl. Phys.* **2005**, *97*, 053304.
31. Malvern, A. R.; Pinder, A. C.; Stacey, D. N. and Thompson, R. C. Self-broadening in singlet spectral lines of helium. *Proc. Royal Soc. London A* **1980**, *371*, 259–278.
32. Woltz, L. A. Quasi-static ion broadening of isolated spectral lines. *J. Quant. Spectrosc. Radiat. Transfer* **1986**, *36*, 547–555.
33. Griem, H. R. Plasma spectroscopy. New York McGraw-Hill, **1964**.
34. Hamdan, A.; Marinov, I.; Rousseau, A. and Belmonte, T. Time-resolved imaging of nanosecond-pulsed micro-discharges in heptane. *J. Phys. D: Appl. Phys.* **2013**, *47*, 055203.
35. Chung, K. J. and Hwang, Y. S. Thermodynamic properties and electrical conductivity of water plasma. *Contrib. Plasma Phys.* **2013**, *53*, 330-335.
36. Eubank, P. T.; Patel, M. R.; Barrufet, M. A. and Bozkurt, B. Theoretical models of the electrical discharge machining process. III. The variable mass, cylindrical plasma model. *J. Appl. Phys.* **1993**, *73*, 7900-7909.
37. Stanek, M.; Musioł, K. and Łabuz S. Experimental determination of transition probabilities in Bi I and Bi II, *Acta Phys. Pol. A* **1981**, *59*, 239–245.

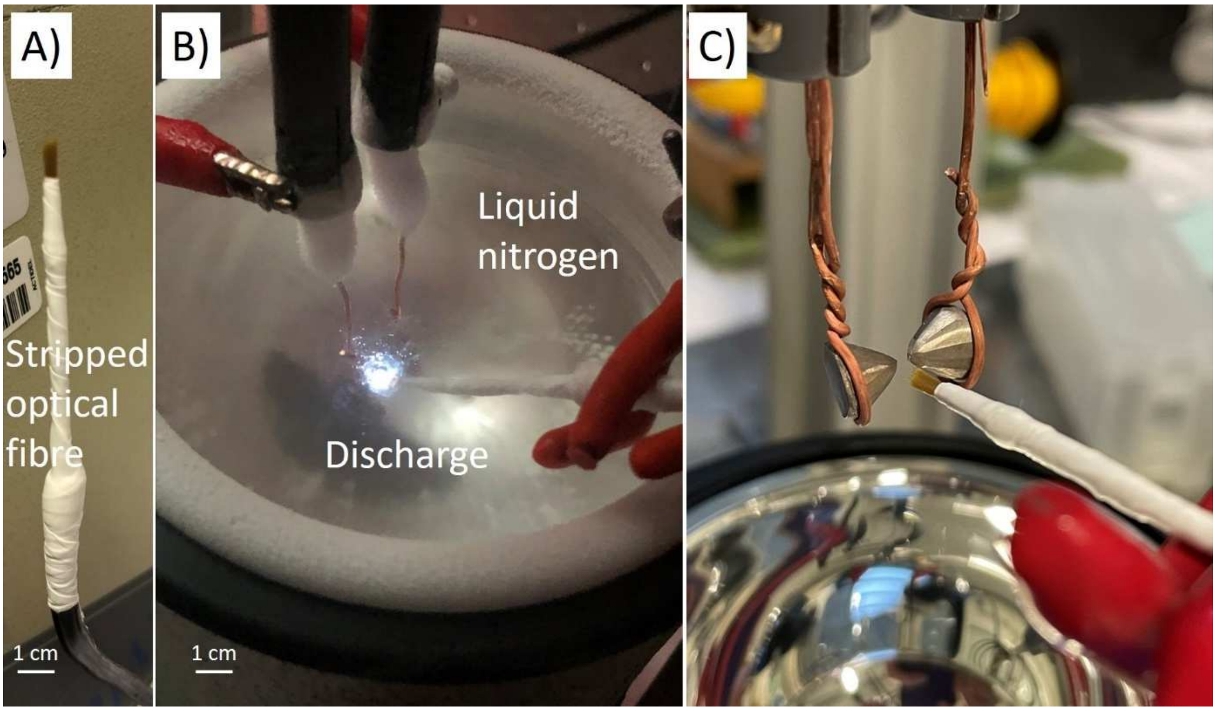

Figure 1: A) Picture of the stripped multi-strand optical fibre. B) Picture of the discharge in liquid nitrogen. C) Picture of the bismuth electrode (the gap distance is set at 100 µm typically during the process – the gap is larger for the picture)

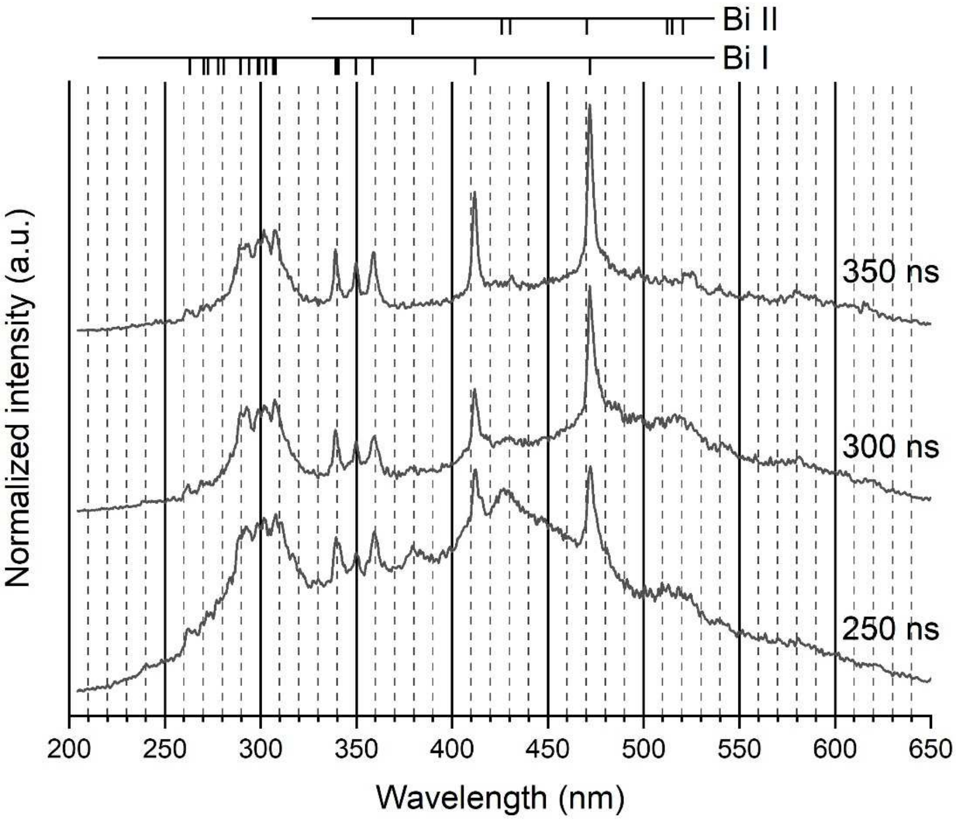

Figure 2. Example of three recorded spectra over the range of wavelengths [200–650 nm]. Ionic lines are clearly visible, despite their weakness. 100 gr. mm^{-1} grating. Integration time: 50 ns.

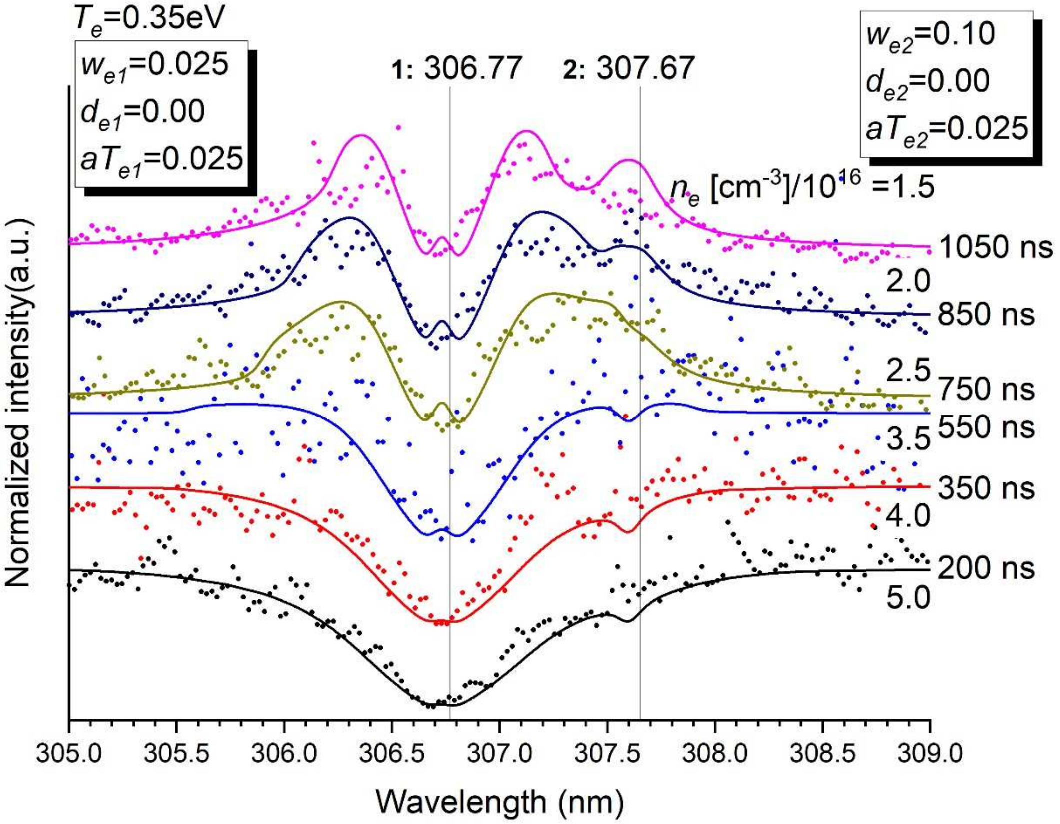

Figure 3: Normalized intensity of the emission of the transitions at 306.77 nm (resonant) and 307.67 nm as a function of time. Stark parameters are given the inset. The electron density n_e in [cm^{-3}]/10^{16} is determined for each time. T_e = 0.35 eV. P = 5 bars.

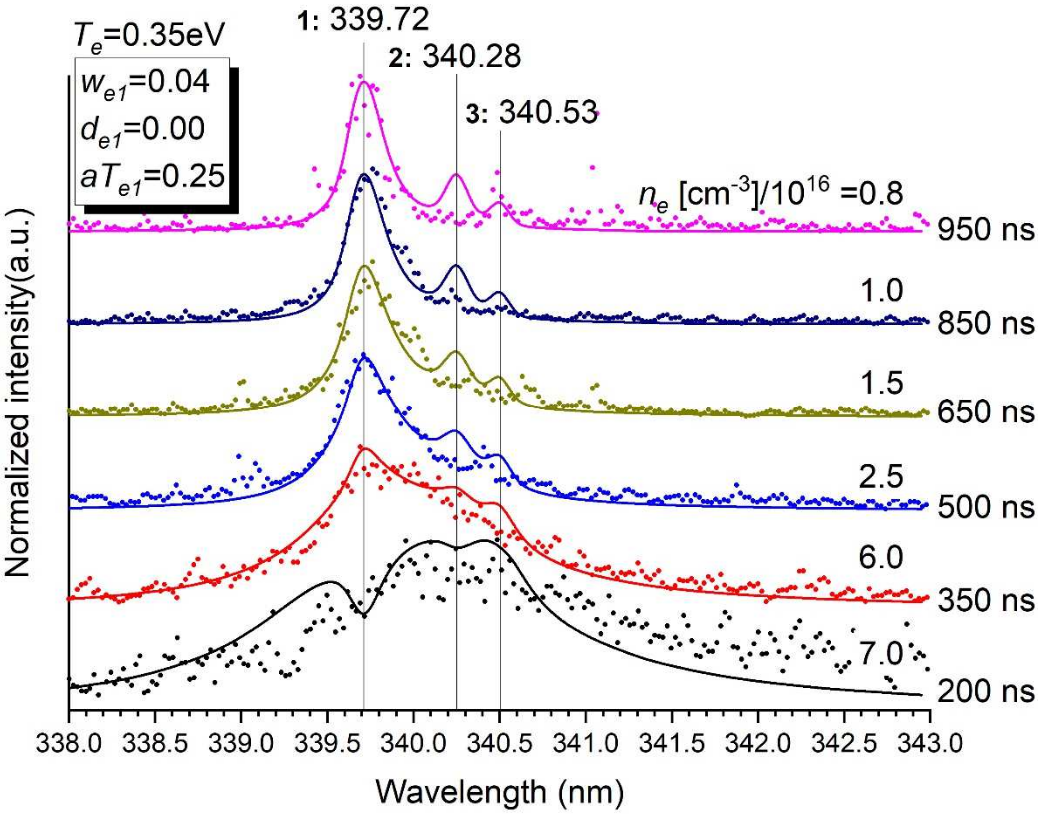

Figure 4: Normalized intensity of the emission of the transitions at 339.72 nm, 340.28 nm and 340.53 nm as a function of time. Stark parameters are given the inset. Data at 250, 300 and 550 ns are too noisy to be exploited. The electron density n_e in [cm^{-3}]/10^{16} is determined for each time. T_e = 0.35 eV. P = 5 bars. Stark parameters for lines 2 and 3 could not be determined with sufficient accuracy to be reported here.

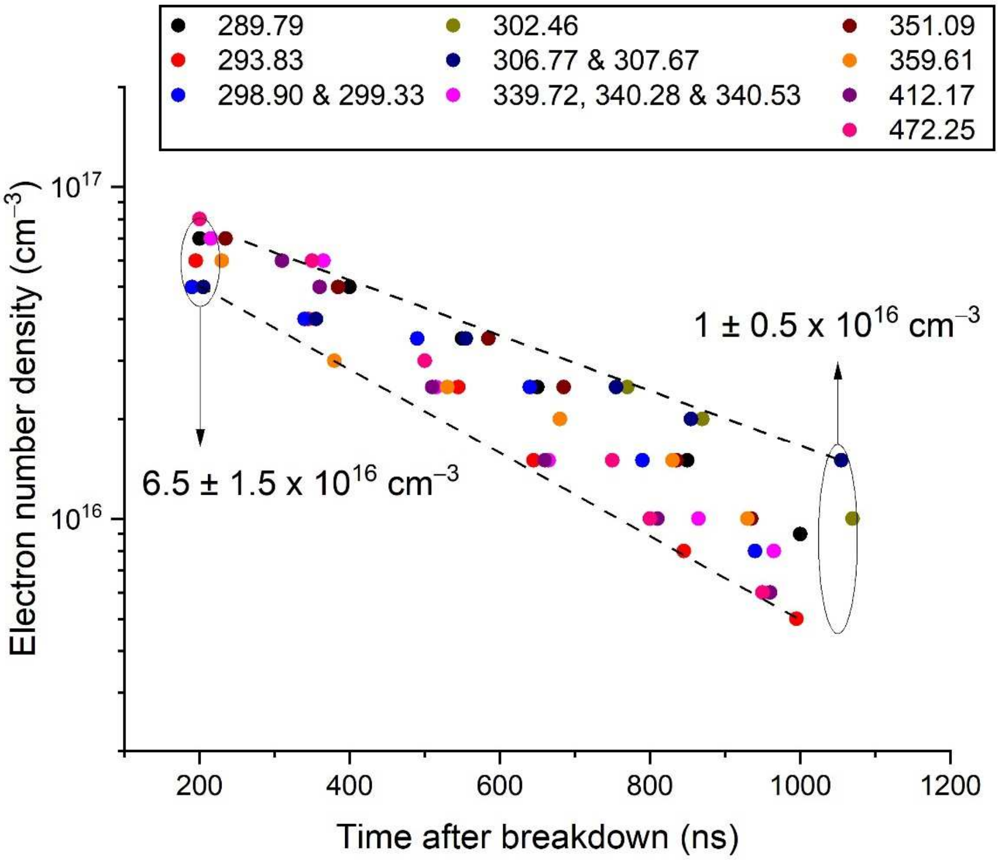

Figure 5: Evolution of the electron number density versus time after breakdown as determined by modelling of some selected Bi I transitions. Dots are slightly shifted in time (from -20 ns to +20 ns) to make them visible.

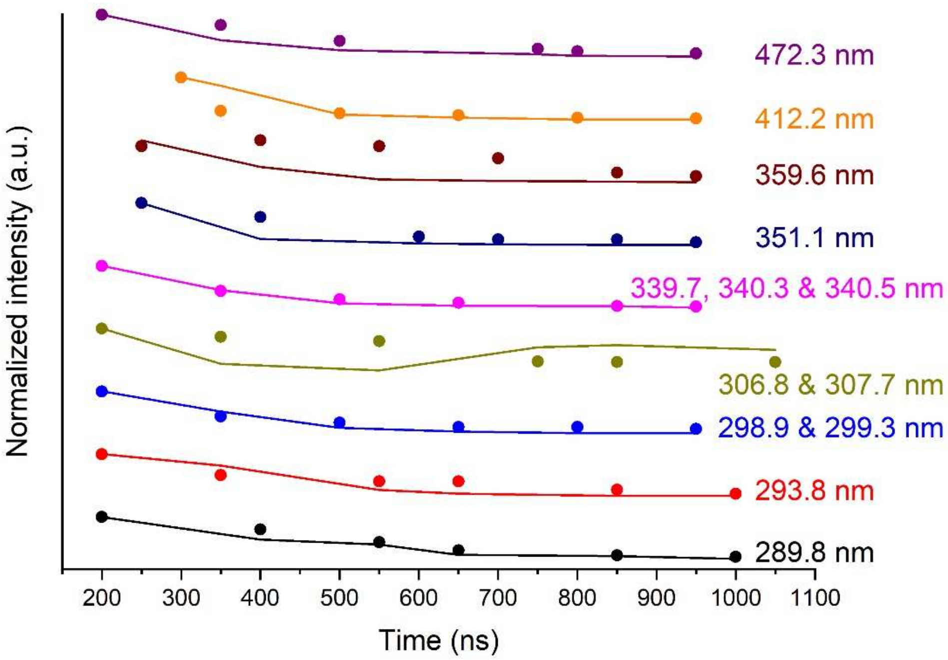

Figure 6: Dots: Normalized parametric intensity of the continuum as a function of time for all the modelled Bi I transitions at the 6 chosen times. Strait lines: Idem for the normalized experimental intensity. 1800 gr. mm^{-1} grating. Integration time: 50 ns.

A)

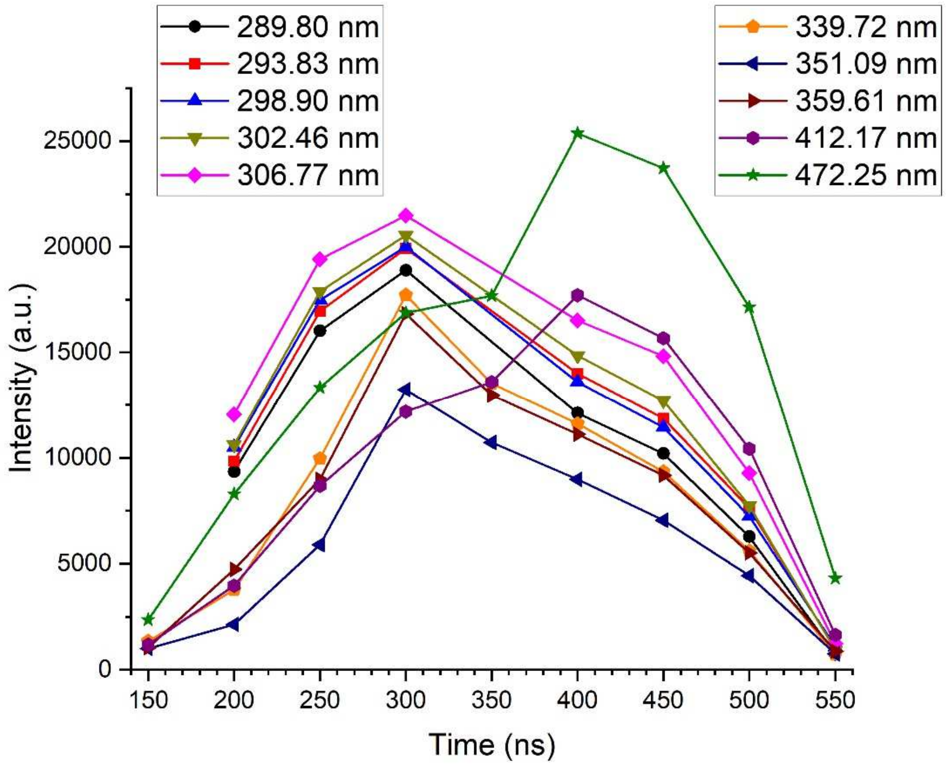

Figure 7: A) Time evolution of the intensity of selected Bi I neutral lines as measured with the 100 B) ^{1} grating. B) Time evolution of the ratio of the intensity of a given line X to the inter he line at 262.79 nm. The dots under "Theory" (put arbitrarily at 570 ns and 650 ns for outliers, *i.e.* ρ >> 1) correspond to the average expected value for a Boltzmann distribution and can be read on the Y-scale. ρ (given by numbers between 0.25 and 158) is the ratio between the theoretical ratio and the average experimental ratio.

Table 1: Basic data used in the model and taken from reference [26, 27]. Acc. is the accuracy of the line (same meaning as NIST). Aul is the transition probability. E_{low} and E_{up} are the energies of the lower and upper levels. J_{low} and J_{up} are the total electronic angular-momentum quantum numbers of lower and upper levels. C'_3 values are deduced from the oscillator strengths taken in [24] and Eq. (8) and C'_6 values are calculated using Eq.(10). w_e, d_e and $a(T_e)$ are data needed in Eq. (16). (see text for details)

	Wavelength (nm)	Rel. Int. (/100)	Obs. Int.	Acc.	A_{ul} (s^{-1})	E_{low} (eV)	E_{up} (eV)	J_{low}	J_{up}	C'_3 (m^3/s)	$C'_6{}^{*}$ (m^6/s)	w_e (nm)	d_e (nm)	$a(T_e)$
Bi I system	262.7904	160	w		4.56×10^{7}	1.4157804	6.1323713	1	1		1.12×10^{-41}			
	269.6748	50	vw		6.20×10^{6}	1.4157804	6.0119775	1	2		9.10×10^{-42}			
	273.0492	17	vw		2.02×10^{7}	2.6856111	7.2249911	0	1		1.63×10^{-39}			
	278.0476	50	vw		3.09×10^{7}	1.4157804	5.8735626	1	0		7.32×10^{-42}			
	280.9615	25	vw		1.34×10^{7}	1.9140062	6.3255610	2	1		1.63×10^{-41}			
	289.7964	410	s	D+	1.53×10^{8}	1.4157804	5.6928439	1	0		5.66×10^{-42}	0.01	0.00	0.35
	293.8297	280	s	D+	1.20×10^{8}	1.9140062	6.1323713	2	1		1.11×10^{-41}	0.05	0.00	0.35
	298.9004	280	s	D+	5.40×10^{7}	1.4157804	5.5625605	1	1		4.69×10^{-42}	0.01	0.00	0.025
	299.3327	60	s	D+	1.45×10^{7}	1.4157804	5.5565801	1	2		4.74×10^{-42}	0.05	0.00	0.025
	302.4618	340	s	D+	8.62×10^{7}	1.9140062	6.0119775	2	2		9.02×10^{-42}	0.025	0.00	0.40
	306.7699**	2300	s	D+	1.67×10^{8}	0	4.0404245	1	0	9.72×10^{-15}	1.18×10^{-42}	0.025	0.00	0.025
	307.6654	30	w	D	3.31×10^{6}	1.4157804	5.4469162†	1	1‡		1.02×10^{-42}	0.1	0.00	0.025
	339.7198	70	s	D+	1.79×10^{7}	1.9140062	5.5625605	2	1		4.69×10^{-42}	0.04	0.00	0.25
	340.2800	9	vw	E	1.50×10^{6}	1.9140062	5.5565801	2	2		4.64×10^{-42}	***	***	***
	340.5330	17	vw	E	6.40×10^{6}	2.6856111	6.3255610	0	1		1.61×10^{-41}	***	***	***
	351.0864	60	s	D+	6.50×10^{6}	1.9140062	5.4444405	2	1		4.04×10^{-42}	0.04	0.00	0.25
	359.6110	27	s	D+	1.93×10^{7}	2.6856111	6.1323713	0	1		1.09×10^{-41}	0.05	0.00	0.20
	412.1704	26	s	D+	1.64×10^{7}	2.6856111	5.6928439	0	0		5.38×10^{-42}	0.05	0.10	0.45
	472.2528	110	vs	C	9.40×10^{6}	1.4157804	4.0404245	1	0		1.02×10^{-42}	0.025	0.04	0.45
Bi II system	379.2564	70	w			9.8060517	13.0742633	2	3					
	425.9413	75	vw			10.1985993	13.1086088	3	4					
	430.1697	70	w			10.1728579	13.0542630	2	3					
	470.5285	60	hd			10.4494435	13.0837049	1	2					
	512.4356	50	vw			11.0062562	13.425090	2	3					
	514.4492	60	vw			8.5715101	10.9808694	0	1					
	520.9325	75	vw			8.6291111	11.0084923	1	2					

*collider: N_2 ; **resonant line ; vw: very weak ; w: weak ; s: strong ; vs: very strong ; hd: hidden ; ***too weak to be estimated ; † unknown level ; ‡ assumed. The estimated accuracies for Stark parameters are: C < 25%, D+ < 40%, D < 50% ; E > 50%.

Table 2: Broadening contributions expressed in pm for different Bi I transitions due to different sources. T_e = 0.35 eV. P = 5 bars. $n_e = 6\times10^{16}$ cm^{-3}. vdW IA : van der Waals impact approximation. QS : quasi-static approximation.

Wavelength	Instrument	Doppler	vdW IA	vdW QS	Resonance	Stark QS
289.7964	100	0.91	3.8	0.5	0	159
293.8297	100	0.92	5.2	1.1	0	794
298.9004	100	0.94	3.8	0.5	0	123
299.3327	100	0.94	3.8	0.5	0	614
302.4618	100	0.95	5.0	0.9		404
306.7699**	100	0.96	2.3	0.1	93.6	307
307.6654	100	0.97	2.2	0.1	0	1228
339.7198	100	1.07	4.9	0.6	0	591
340.2800	100	1.07	4.9	0.6	0	368
340.5330	100	1.07	4.9	0.6	0	123
351.0864	100	1.10	8.6	2.3	0	591
359.6110	100	1.13	7.7	1.6	0	711
412.1704	100	1.30	7.6	1.0	0	850
472.2528	100	1.49	5.1	0.2	0	425

SUPPLEMENTARY FILE

Study by Optical Spectroscopy of Bismuth Emission in a Nanosecond-Pulsed Discharge Created in Liquid Nitrogen

Anna Nominé[1], Cédric Noel[1], Thomas Gries[1], Alexandre Nominé[1,2], Valentin Milichko[2] and Thierry Belmonte[1]

[1] Université de Lorraine, CNRS, IJL, F-54000 Nancy, France

[2] ITMO University, St. Petersburg 197101, Russia

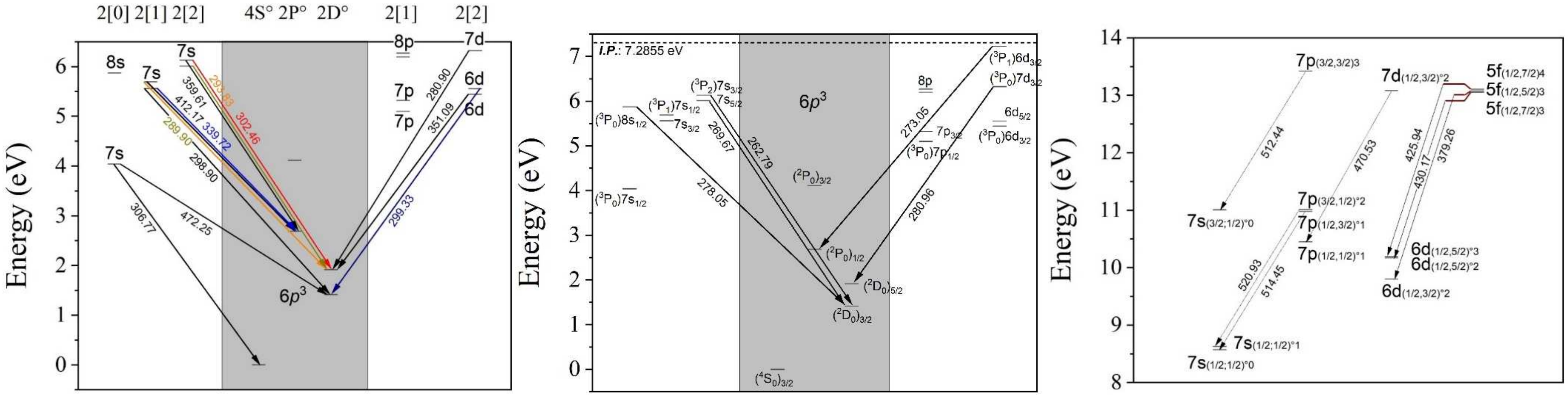

Supplemental material 1: Bi I and Bi II Grotrian diagrams and observed optical transitions.

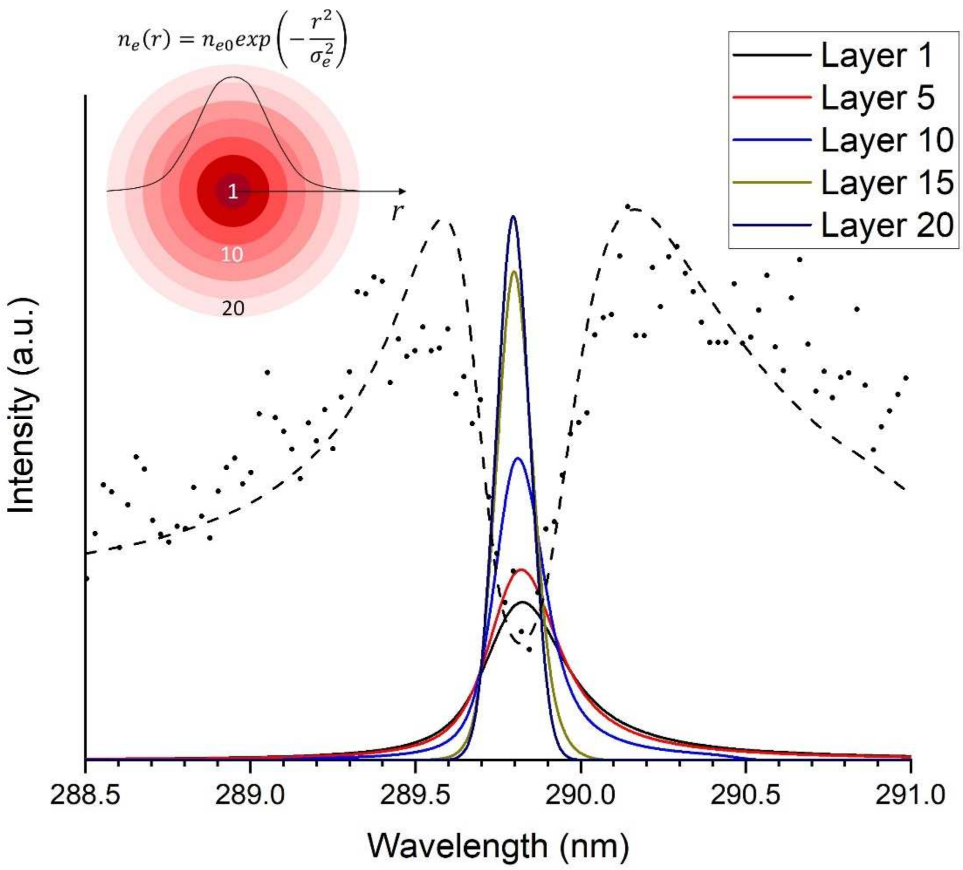

Supplemental material 2: Emission intensities of the transition at 289.80 nm in 5 chosen layers of the optical model leading to the profile given by the dashed line. Dots are experimental data. Photons at central wavelength are trapped by atoms in the lower level and take longer to escape the medium, leading to a hole in the distribution. We do verify that emission lines become narrower and symmetrical as the electron density decreases from layer 1 to layer 20.

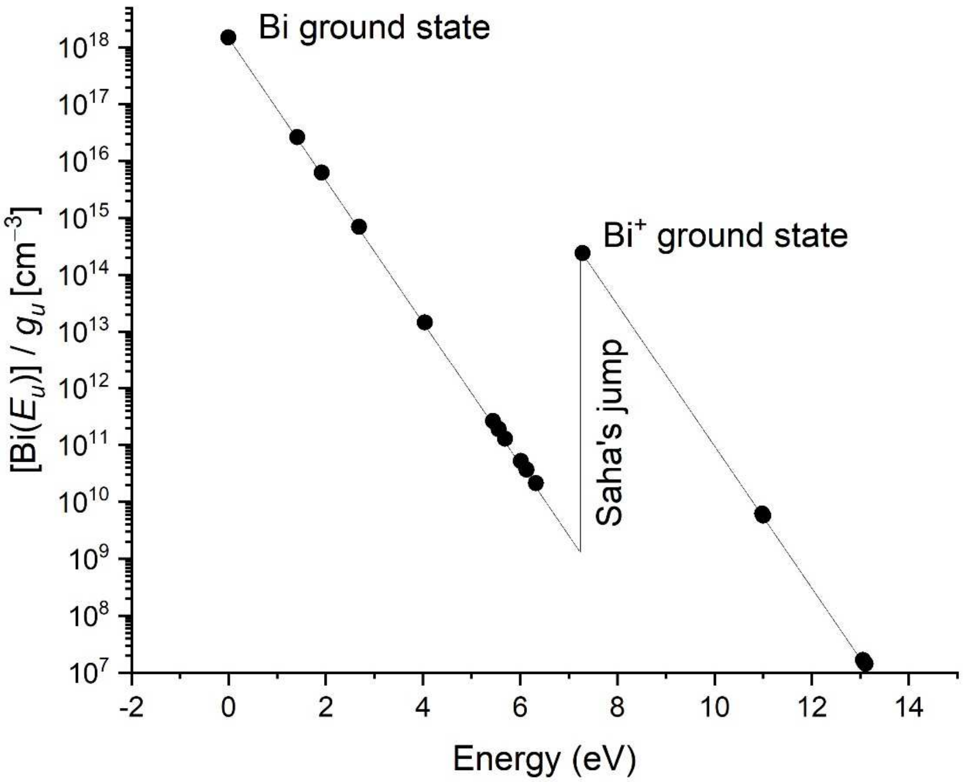

Supplemental material 3: Boltzmann plot showing the distribution in energy of the Bi I and Bi II states identified in this work.

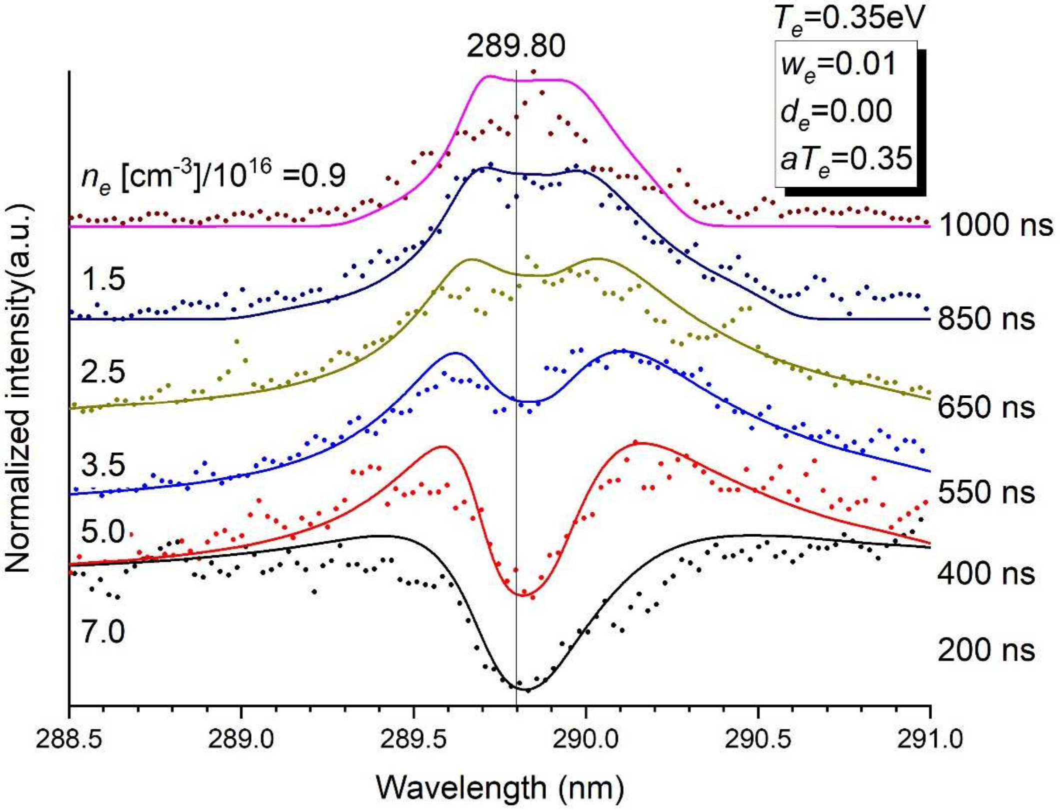

Supplemental material 4a: Normalized intensity of the emission of the transition at 289.80 nm as a function of time. Stark parameters are given the inset. The electron density n_e in [cm^{-3}]/10^{16} is determined for each time. T_e = 0.35 eV. P = 5 bars.

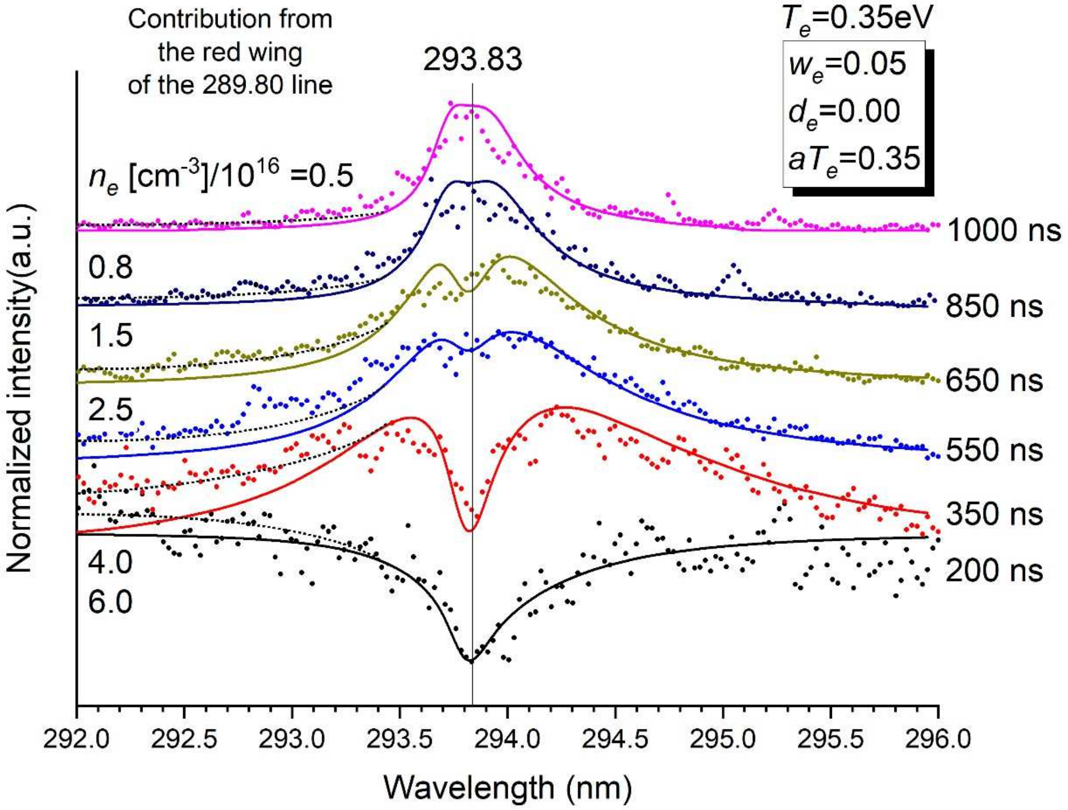

Supplemental material 4b: Normalized intensity of the emission of the transition at 293.83 nm as a function of time. Stark parameters are given the inset. The blue part of the line is perturbed by the red wing of the 289.80 transition, which must be included for a correct description of that part of the spectrum. The electron density n_e in [cm^{-3}]/10^{16} is determined for each time. T_e = 0.35 eV. P = 5 bars.

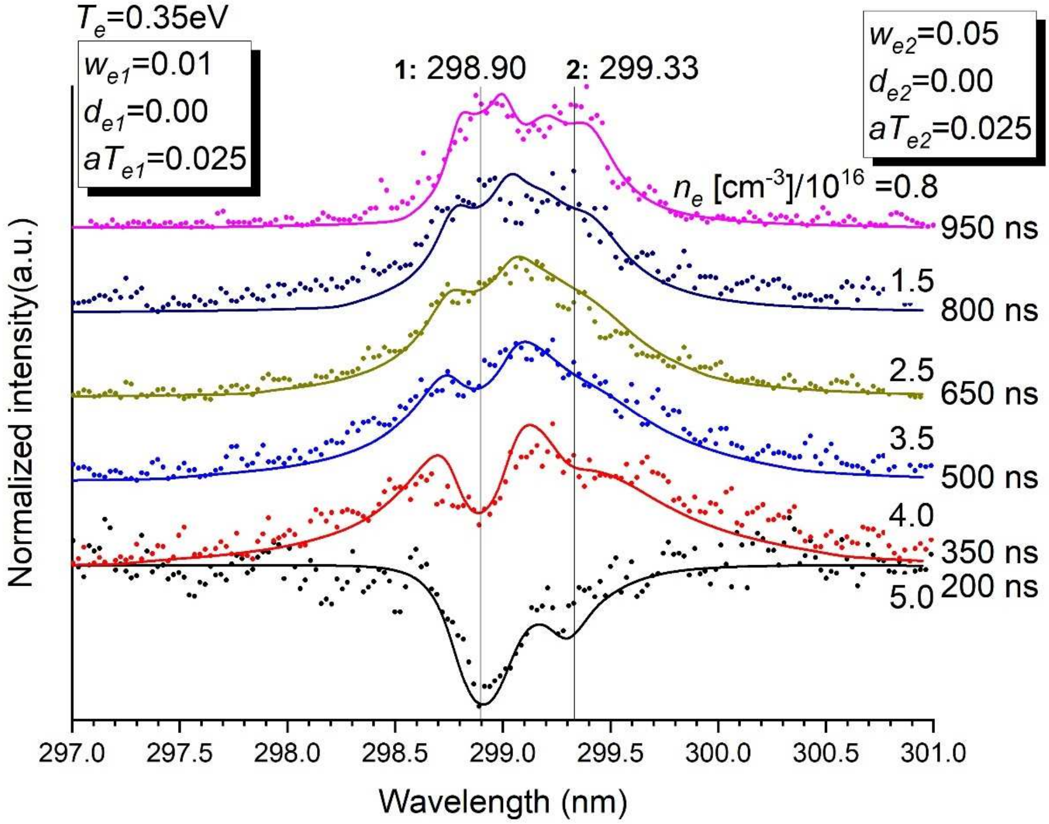

Supplemental material 4c: Normalized intensity of the emission of the transitions at 298.90 nm and 299.33 nm as a function of time. Stark parameters for each transition are given the insets. The electron density n_e in [cm^{-3}]/10^{16} is determined for each time. T_e = 0.35 eV. P = 5 bars.

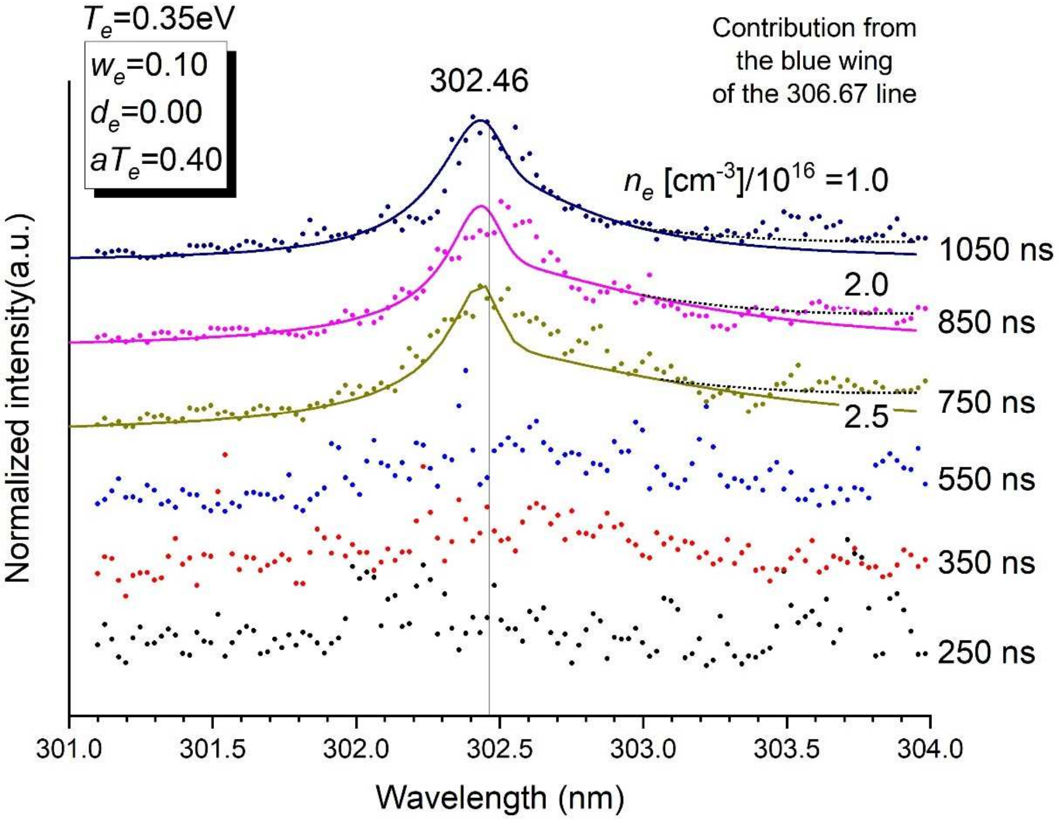

Supplemental material 4d: Normalized intensity of the emission of the transition at 302.46 nm as a function of time. Stark parameters are given the inset. The red part of the line is perturbed by the blue wing of the 306.67 transition, which must be included for a correct description of that part of the spectrum. Data at 250, 350 and 550 ns are too noisy to be exploited. The electron density n_e in [cm^{-3}]/10^{16} is determined for each time. T_e = 0.35 eV. P = 5 bars.

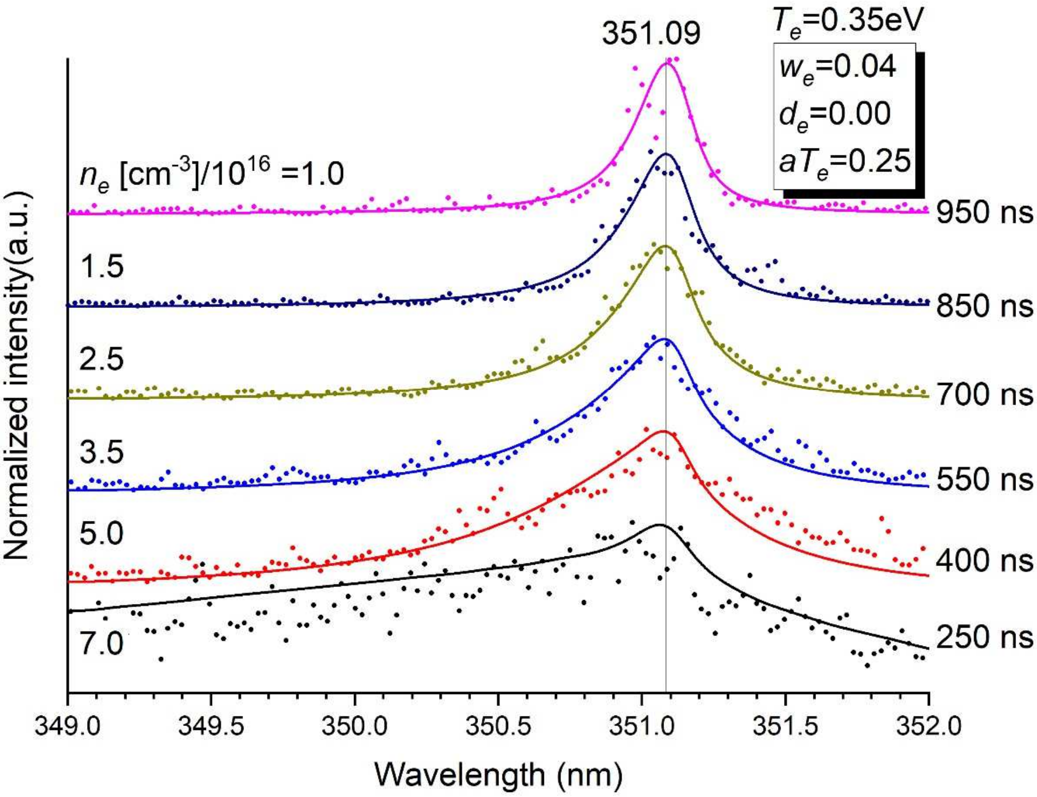

Supplemental material 4e: Normalized intensity of the emission of the transition at 351.09 nm as a function of time. Stark parameters are given the inset. Contrary to other lines, it is the red wing of the transition that is asymmetric. The electron density n_e in [cm^{-3}]/10^{16} is determined for each time. T_e = 0.35 eV. P = 5 bars.

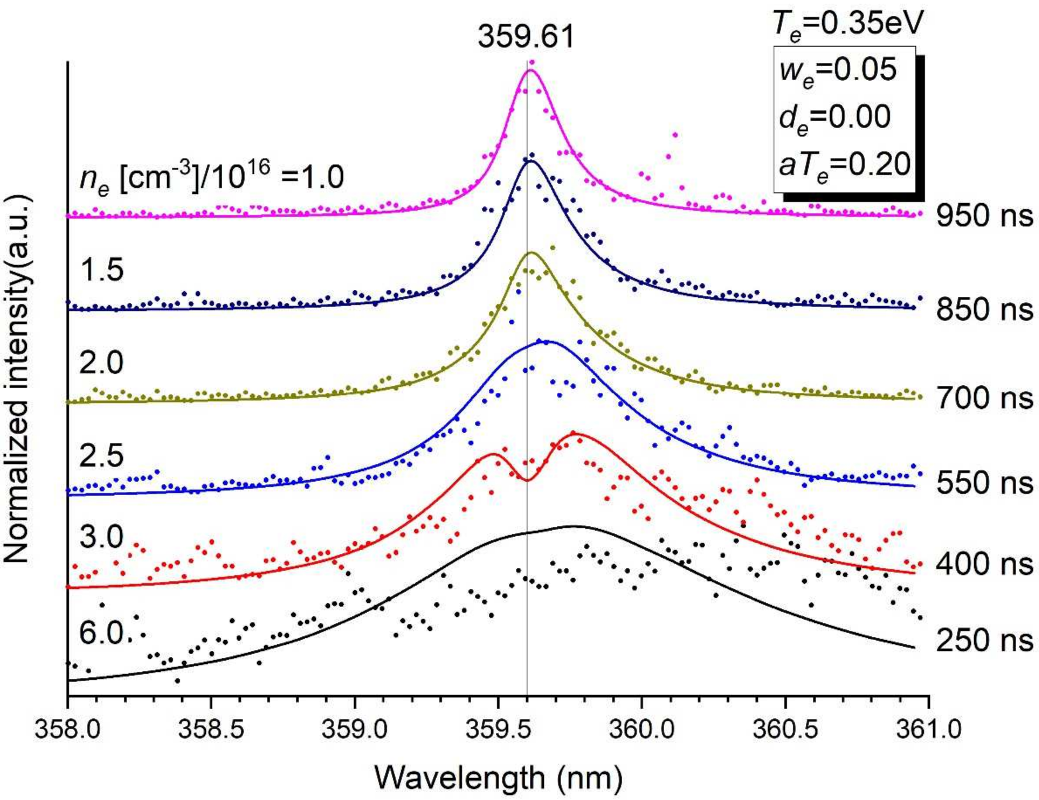

Supplemental material 4f: Normalized intensity of the emission of the transition at 359.61 nm as a function of time. Stark parameters are given the inset. The electron density n_e in [cm^{-3}]/10^{16} is determined for each time. T_e = 0.35 eV. P = 5 bars.

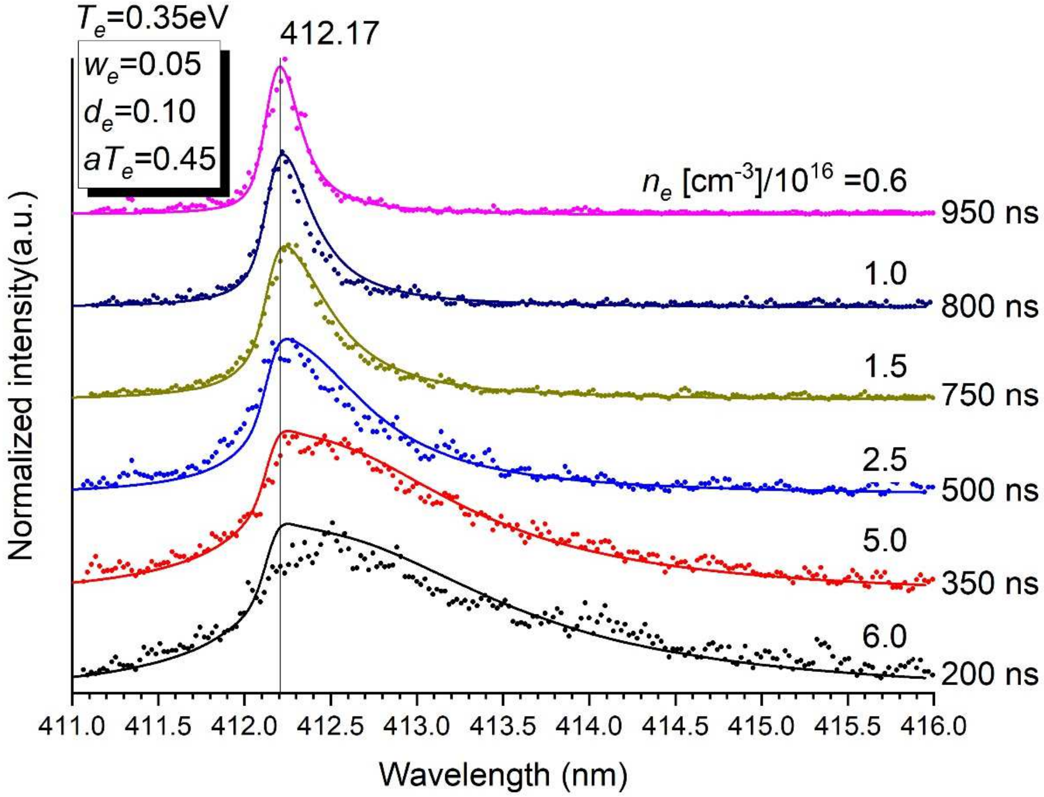

Supplemental material 4g: Normalized intensity of the emission of the transition at 412.17 nm as a function of time. Stark parameters are given the inset. The electron density n_e in [cm^{-3}]/10^{16} is determined for each time. T_e = 0.35 eV. P = 5 bars.

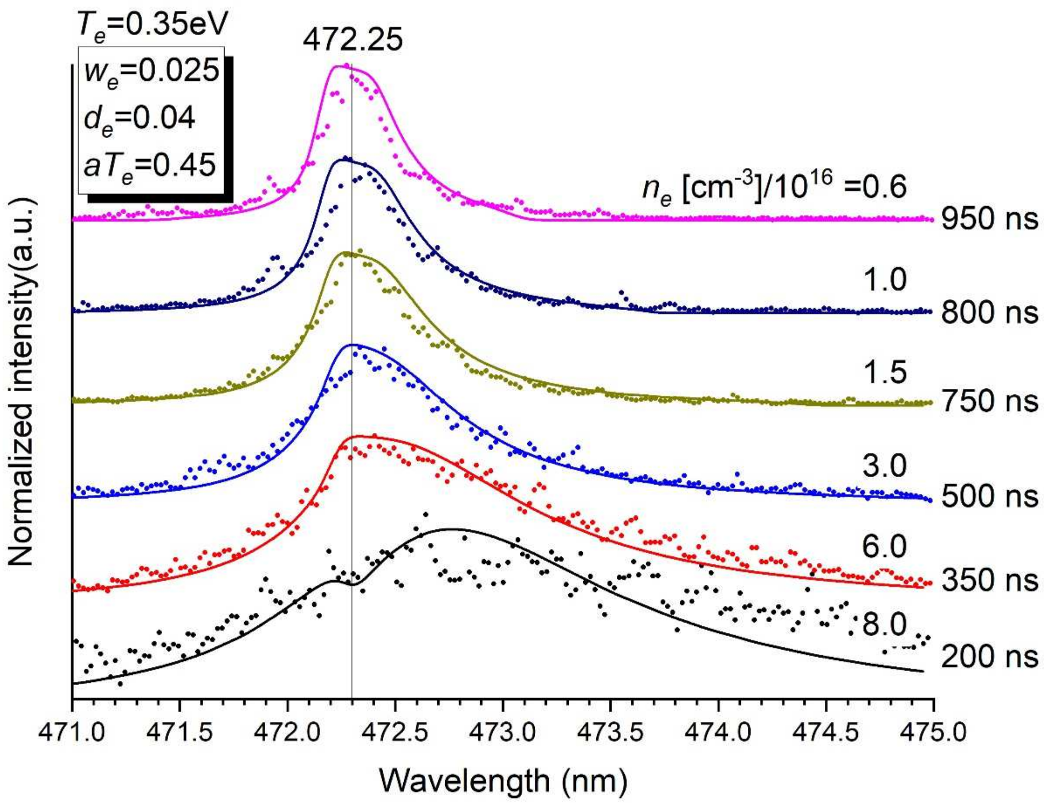

Supplemental material 4h: Normalized intensity of the emission of the transition at 472.25 nm as a function of time. Stark parameters are given the inset. The electron density n_e in [cm^{-3}]/10^{16} is determined for each time. T_e = 0.35 eV. P = 5 bars.

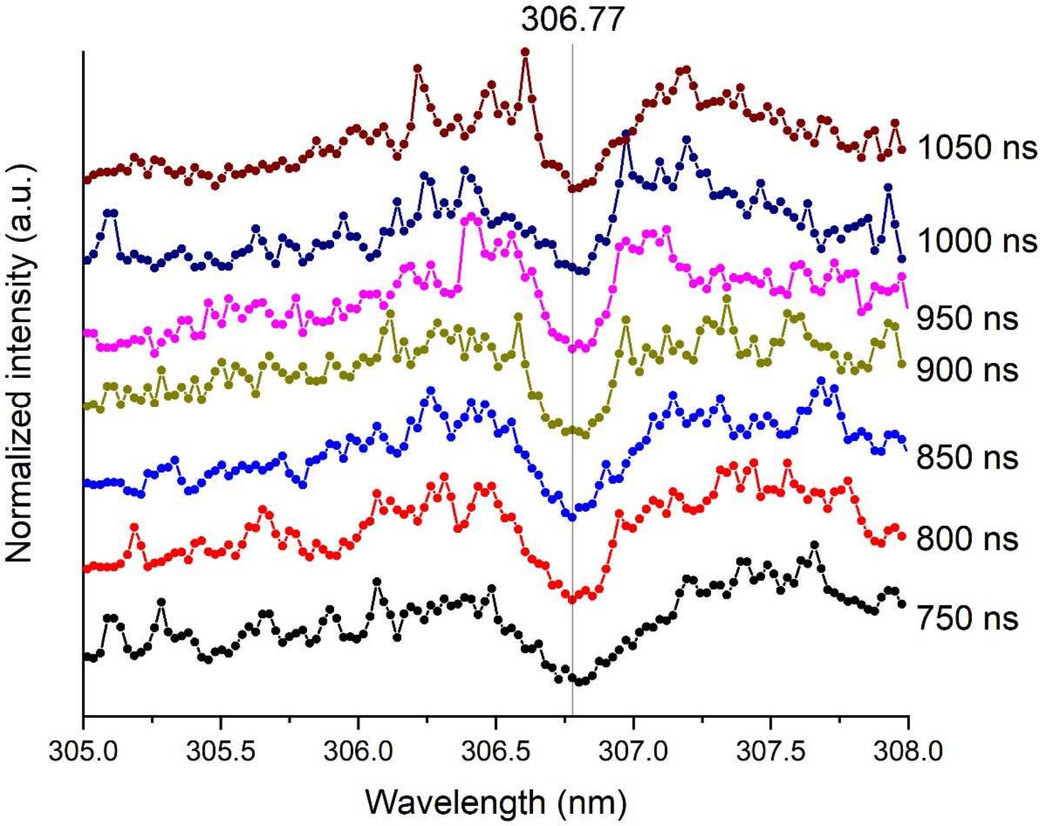

Supplemental material 5: Detail of all experimental spectra recorded after 750 ns (where this phenomenon is the most likely – see **Figure 3** in the main text) where the possible double reversal is theoretically expected to occur (transition at 306.77 nm). The reader is invited to form his own opinion.

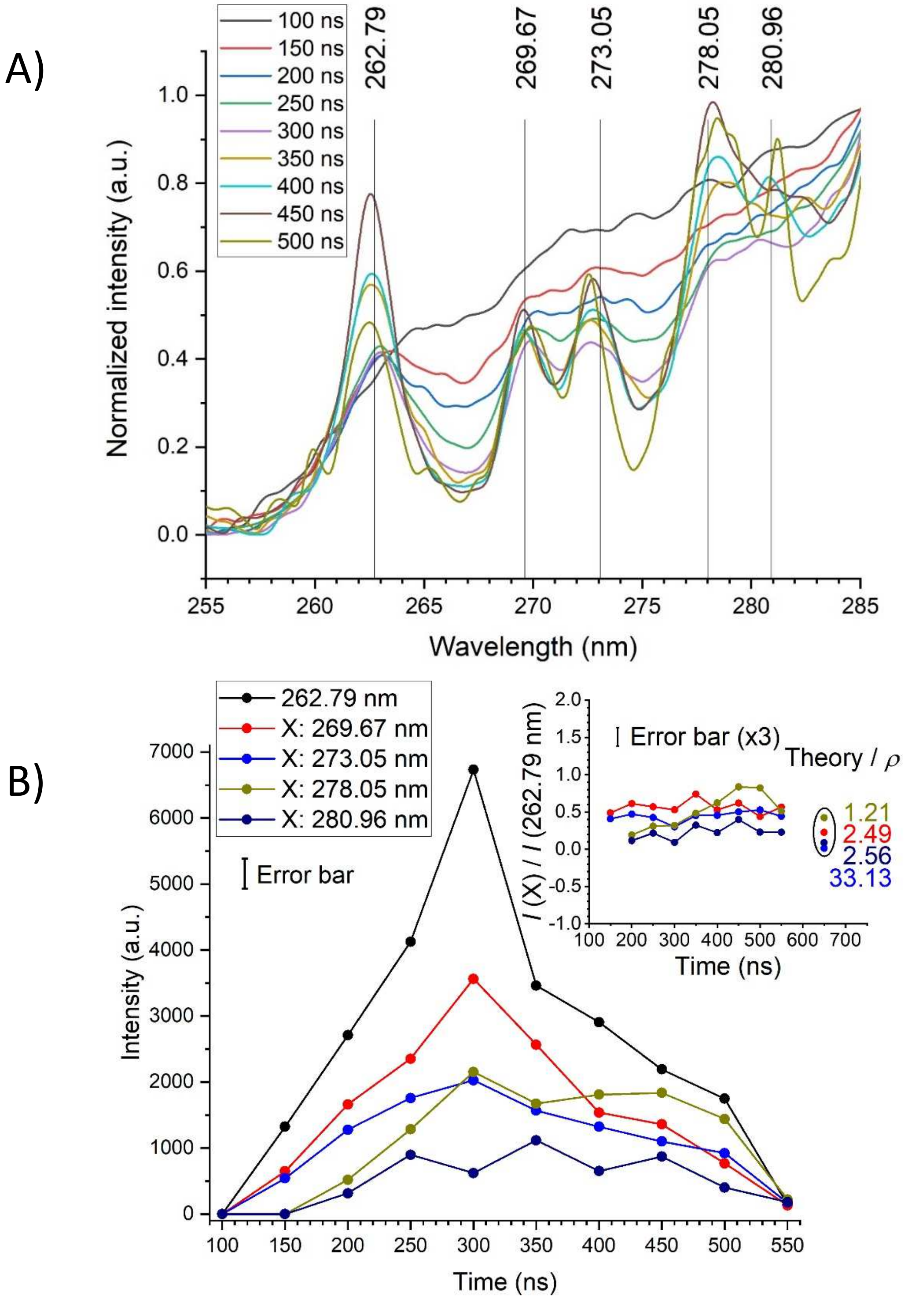

Supplemental material 6: A) Evidence of Bi I emission with normalized intensities of 1 weak (at 262.79 nm) and 4 very weak lines in the UV region. 100 gr. mm^{-1} grating. Integration time: 50 ns. These lines are too weak to be observed with the 1800 gr. mm^{-1} grating. B) Time evolution of these lines (true intensities) as measured with the 100 gr. mm^{-1} grating. Insert: Time evolution of the ratio of the intensity of a given line X to the intensity of the line at 262.79 nm. "Theory" and ρ have the same meaning as in **Figure 7**.

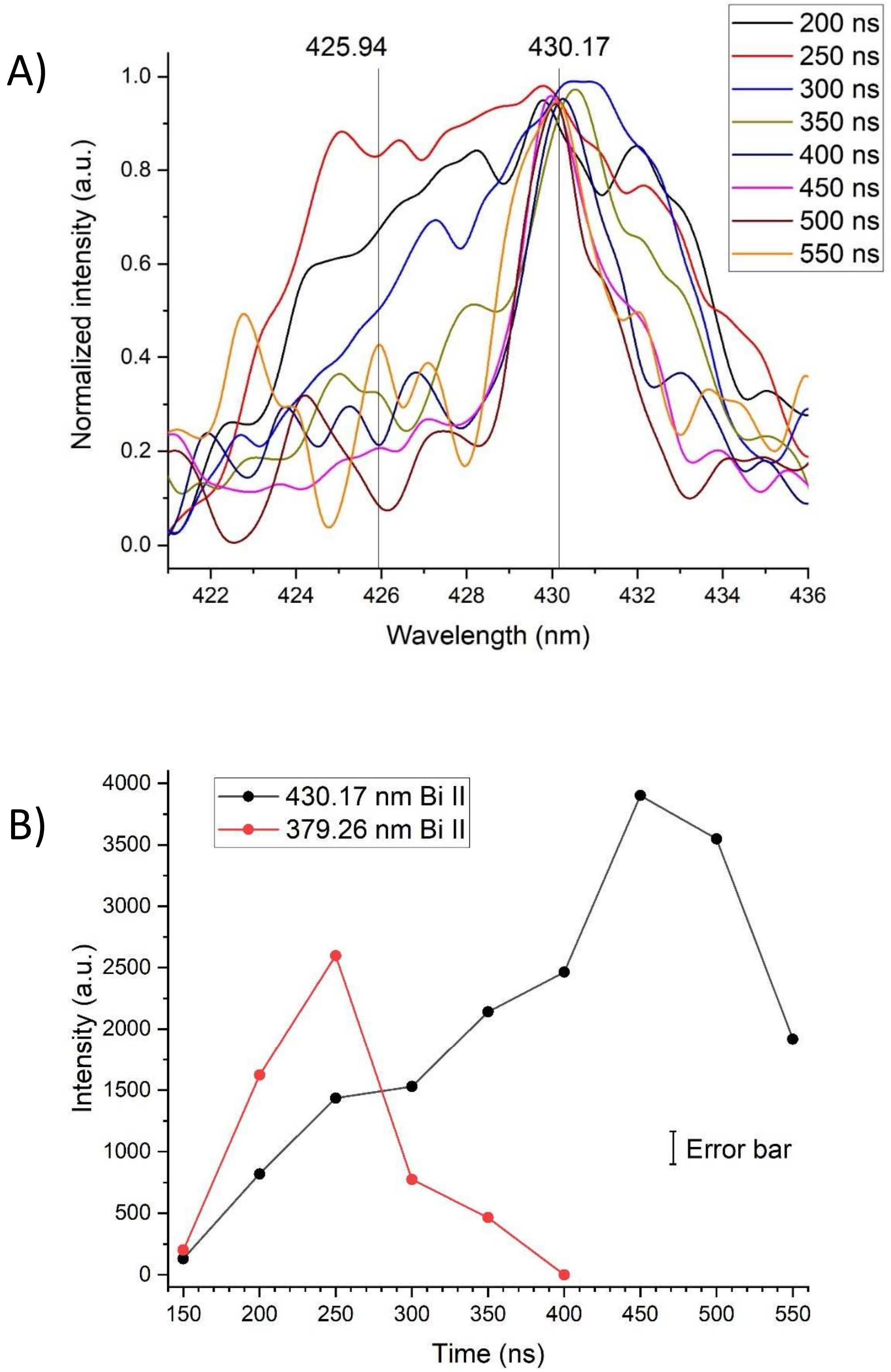

Supplemental material 7: A) Evidence of Bi II emission of 1 weak line(at 430.17 nm) in the UV region. 100 gr. mm^{-1} grating. Integration time: 50 ns. This line (and the one at 379.26 nm) are too weak to be observed with the 1800 gr. mm^{-1} grating. B) Time evolution of these lines as measured with the 100 gr. mm^{-1} grating.